CHARACTERIZATION OF MICROSCOPIC IMPACT DAMAGE IN CFRP LAMINATES WITH TOUGHENED INTERLAYERS

by

ROZAINI BIN OTHMAN

A thesis submitted in fulfillment of the requirements
for the degree of
Doctor of Engineering
in Graduate School of Science and Engineering
Ehime University

June 2017

ACKOWLEDGEMENT

In the name of Allah, Most Gracious and Most Merciful. I would like to express my sincere thanks and gratitude to my supervisor, Prof Dr Keiji Ogi, for his guidance, support, advice and encouragement given throughout my doctoral journey at Ehime University. I would also like to express my gratitude to Prof Dr Manabu Takahashi and Prof Dr Daisuke Yanagihara for their valuable input and comments to improve the content of my thesis.

An appreciation is due to Associate Professor Dr Mitsuyoshi Tsutsumi, Assistant Professor Dr Koichi Mizukami and the rest member of Mechanic of Materials Laboratory especially Kensuke Murakami, Sudarsono and Baso Nasrullah for their help and support during this research work.

I would also like to thank Government of Malaysia as well as Universiti Teknologi MARA for providing financial support. My sincere gratitude is also extended to member of Matsuyama Islamic Cultural Center (MICC), ISMA Jepun and Malaysian Community in Matsuyama for their encouragement, *ukhuwwah* and companionship throughout my stay in Japan.

I should like to express my deepest appreciation to my family for their endless support and encouragement given over such a long period of time especially my parent who has tried their best in providing me with the best education. A special appreciation

to my beloved wife, Zaiton Binti Din, for all the care, support, encouragement and understanding throughout these long and hard years and to my four children, Ammar, Aleeya, Anas and Awfa - all of whom has made life in this foreign country bearable. Finally to everyone I knew, whose names are too many to be listed, thank you very much for everything.

Thank you very much.

~Rozaini Bin Othman~
June 2017.

SUMMARY

This study aims at characterization of microscopic impact damage of CFRP laminates with toughened interlayers. In general, CFRP has been applied to various engineering application due to its superior properties such as high stiffness and strength. For example, CFRP is employed in aircraft structure such as wings, turbo-fan engines and a fuselage. Nonetheless, it is still vulnerable to damage induced by low-velocity and high-velocity impact. The damage due to low-velocity impact can be classified either barely visible impact damage (BVID) or clearly visible impact damage (CVID). In the former case, even though a small dent is created on the laminate surface, significant damage including matrix cracking and delamination is often generated inside the laminate.

On the contrary, high-velocity impact creates clear evidence such as a crater on the surface besides more catastrophic failure than low-velocity impact. In the event of high velocity impact, punching failure, fibre failure, matrix cracking and delamination are considered as main damage mechanism that occurred in composite materials. In general, it is supposed that punching failure is initially generated and followed by fibre breakage before delamination occurs at the back side interfaces of the laminate. The relative thickness of each damage process depends on overall laminate thickness.

Accordingly, CFRP laminates toughened with interlayers have been developed to improve interlaminar fracture toughness to constrain initiation and propagation of delamination. Thus far, only a few study has been carried out regarding comparison of microscopic damage in CFRP laminates toughened with interlayers between low- and high-velocity impacts. Furthermore, to the author knowledge, no numerical model has been developed to reproduce the impact damage processes in this type of laminate. Therefore, this study aims to thoroughly characterize and model the microscopic damage of CFRP with toughened interlayers subjected to both low- and high-velocity impacts through experiment characterization and numerical modelling.

The material used in this study was T800S/3900-2B (Toray Industries Inc.), CFRP laminates toughened with interlayers, employed in aircraft structure (B787). The fiber strength of this material is about 10% higher than that of T800H/#3900-2 used in B777 aircraft. The stacking sequence was cross-ply lamination $[0^0/90^0]_{2s}$. First, low-velocity impact testing was performed by using a drop-weight apparatus developed in the laboratory. Meanwhile, high-velocity impact testing was carried out using a ballistic impact testing machine. The damage observed in the experiment was then reproduced via numerical modelling using commercial finite element analysis (FEA) software (ABAQUS/Explicit). In addition, a user subroutine program (VUMAT) was also incorporated in the FEA software for failure modelling. The laminate consisting of the

base ply and the interlayer was modelled as elastic solid elements, whereas the impactor was modelled as a rigid body. The delamination was considered by introducing cohesive elements which were inserted not only within the base ply, but also between the base ply and the interlayer to reproduce both intralaminar and interlaminar delaminations.

It is found from the experiment results that the splitting cracks on the front surface of the laminate propagate in the fiber direction in the high-velocity impact. In contrast, in the low-velocity impact, the cracks normal to the fiber direction are generated on the front surface. The cracks on the front surface are generated due to high compressive stress in the fiber direction ($0°$-direction) during the impact. The degree of damage is relatively large in the high-velocity impact even though the deformation is localized. In contrast, in the low-velocity impact, the damage is relatively mild because the ratio of dissipated energy to incident impact energy is larger than that in the high-velocity impact.

In addition, the interlaminar delamination tends to propagate in the fiber direction for both impacts, resulting in a galaxy shape delamination. It is also interesting to note that not only the interlaminar but the intralaminar delaminations are generated inside the laminate. With regard to the role of toughened interlayers, the interlayers suppress the delamination when the incident impact energy is smaller than the threshold value (approximately 0.18 J). Furthermore, the high fracture toughness of the interlayers sometimes produces the transition of interlaminar delamination to intralaminar delamination.

Apart from experimental characterization, numerical modelling was also successfully developed. The comparison between experiment and numerical modelling indicates that the present numerical modelling can reproduce the damage pattern including intralaminar delamination. The simulation considering both interlaminar and intralaminar delaminations gives better agreement with the experiment result of the deflection rate in the deflection-time curve.

In conclusion, the novel finding in this research is the generation of intralaminar delamination in this type of laminate which is never observed in conventional CFRP laminates. Furthermore, the simulation with cohesive elements which express both intralaminar and interlaminar delaminations provides better result than the simulation with cohesive elements for interlaminar delamination only.

TABLE OF CONTENTS

LIST OF FIGURES

10

LIST OF TABLES

CHAPTER 1: INTRODUCTION

1.1 Background

Advanced composite materials have been used in many applications due to its favourable properties such as specific strength and stiffness. For instance, the adoption of carbon fiber reinforced plastics (CFRPs) as a major contribution to the aircraft structures in the late 1960s such as trim tabs, spoilers, rudders, and doors. During this time, CFRPs employed brittle epoxy resin as a matrix material resulting poor tolerance to low-energy impact due to runaway debris thrown up by the aircraft wheels and impact during manufacture or subsequent maintenance. However, the properties of the CFRP has been improved since then by introducing newer epoxy resin system as well as utilizing thermoplastic material as matrix, for example, polyether-ether-ketone (PEEK) [1].

During 1980s, CFRP was applied in a vertical tail of aircraft as representative for an advanced composite materials. The recent generation of airplanes used composite materials for all main wings and fuselages, leading to superior fuel efficiency and life sustainability [2]. The new Dreamliner 787 was designed almost entirely with high performance carbon fiber materials including the stabilizers, wings and fuselages, which represents 50% of aircraft structural weight. Furthermore, the fuel efficiency was

improved nearly 20% from previous Boeing's top selling aircraft B777 [3]. Figure 1.1

depicts the materials used in Dreamliner 787 body [4].
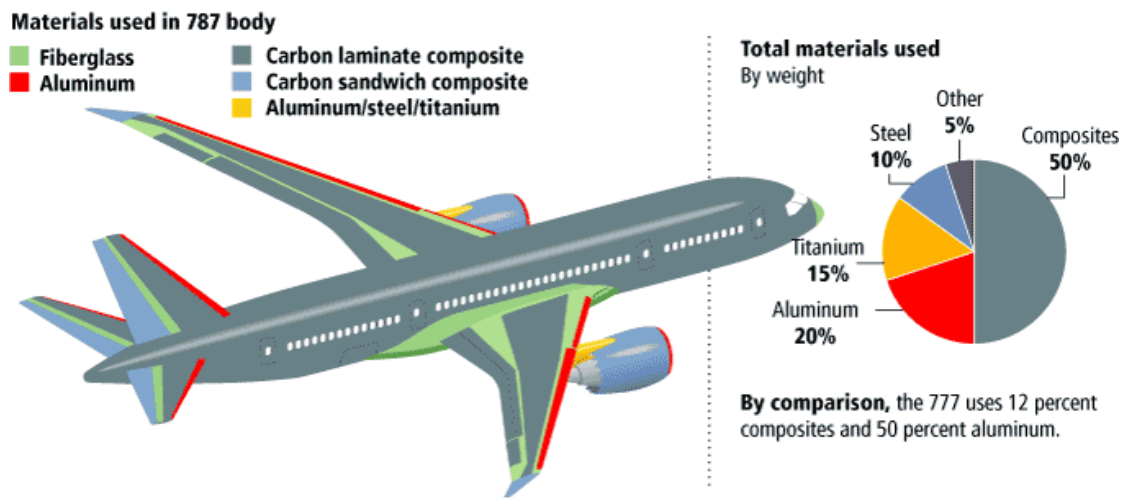
Figure 1.1: Materials used in Dreamliner 787 body [4].

Generally, the composite materials are produced by laying up the thin resin

impregnated and aligned fiber layers (also known as prepreg) with optimized fiber

direction in each layer using autoclave [2]. The composite laminated structures are

reinforced by fibers only on the plane and there is no reinforcement in through-thickness

direction. Thus, the interlaminar strength in laminated composite materials is still one of

the design limiting factor for the laminate structures [5]. In order to improve the

interlaminar fracture toughness, an interlayer is often introduced by replacing the resin at

prepreg surface to a tougher system such as the inclusion of thermoplastic particles [6].

It has been reported that Mode I and Mode II interlaminar fracture toughness improved after adding the tough adhesive layers [7].

Boeing published material specifications in early 1980s that emphasized the impact resistance with a major application to primary structures. Compression after impact (CAI) was chosen as damage tolerance index and has to increase two folds from the conventional materials. In order to satisfy the requirement, it is necessary to improve the impact resistance of the matrix resin maintaining heat resistance while improving the strength of the reinforced fibers significantly. The technological issue was to achieve both hot-wet characteristics and impact resistance characteristics which were mutually exclusive and trade off each other.

Apart from CAI, the delamination growth is also a common failure in composite laminates induced by impact loading and need to be addressed. The delamination propagation could be prevented by increasing the toughness of the interlayer at matrix resin zone. Since there is a correlation between the CAI and delamination area, it is believed that CAI can be improved by adopting similar approach as to halt delamination growth.

Therefore, new particulate interlayer toughening technology was developed to improve the toughness at the interlayer. This technology was achieved by combining

thermoset resin (epoxy) and thermoplastic particles. When the impact is subjected to the laminate, crack propagates through the interlayer zone and destroying the thermoplastic particles to consume the energy, hence preventing the crack to further propagate. Epoxy resin is used due to high elastic modulus, good processability and heat resistance, whereas thermoplastic particles possess high fracture toughness. Epoxy resin is used as base matrix resin and thermoplastic particle is dispersed in both sides of prepreg.

In this regard, new epoxy matrix resin, 3900-2, was developed by Toray Industries Inc. that exhibits an excellent impact resistance and no degradation in heat resistance when laminated. Furthermore, high performance carbon fibers, TORAYCA T800H, which the strength is 50% higher than standard grade carbon fibers, TORAYCA T300 was also developed prior to 3900-2 epoxy resin.

As a result, high toughness laminate TORAYCA Prepreg P2302 was realized by combining high strength carbon fiber, T800H and high toughness epoxy resin, 3900-2. This material was successfully passed the specification of high toughness materials by Boeing, thus, it was applied in primary structures of Boeing B777 [8].

As mentioned earlier, in a development of Boeing 787 Dreamliner, the composites account for 50% of aircraft's structural weight and most of the composites are from Toray Industries's trademark TORAYCA 3900-series highly toughened carbon fiber reinforced

epoxy. The carbon fiber used is T800S type (intermediate modulus) and it is different from the previous T800H with a better modulus elasticity and strength. It is also the result of improved carbon manufacturing processes resulting in higher production rate and better availability [9]. Figure 1.2 depicts the prepreg of CFRP toughened with interlayer.

1.2   Problem Statement

Numerous studies have been carried out with regard to CFRP subjected to impact loading. For example, comparing the impact response and damage between low-velocity and high-velocity impact [10][11][12], effect of resin and fiber properties on impact damage [13][14][15], effect of impact damage on mechanical properties [16][17][18].

The studies demonstrate that even though CFRP has a superior elastic strength, it is still vulnerable to impact loading and the damage generated is different between low-velocity and high-velocity.   As such, a number of methods have been introduced to improve the impact damage resistance of CFRP. For instance, toughened interlayer by using particle [19][20], film insertion [21][22], toughened interlayer by using nano-fibers [23]. In addition, the damage mechanisms may also differ amongst the laminate of different toughening method. Therefore, it is essential to characterize the damage mechanisms for assessing the effectiveness of the toughening method to improve the

impact resistance.

Despite experimental characterization, several numerical models have been proposed by various researchers to model the damage mechanisms of CFRP laminates due to impact [24][25][26][27][28]. All types of failures such as delamination, fiber breakage, matrix cracking were considered in the modelling.

To date, there is only a few study has been carried out regarding microscopic damage of CFRP laminate toughened with interlayers when subjected to low- and high-velocity impacts. Bull et al. [20], has made a good start by elucidating the microscopic damage at low-velocity impact. Morita et al. [11][12], on the other hand, studied the comparison impact damage of CFRP laminate with toughened interlayers between low-velocity and high-velocity impacts. However, the damage is not thoroughly characterized. At present, to the author knowledge, no numerical model has been developed to reproduce the damage processes in this type of laminate.

Therefore, this study aims to thoroughly characterized and model the microscopic damage of CFRP laminates with toughened interlayers when subjected to both low- and high-velocity impacts by using experiment characterization and numerical modelling. The overall research methodology is depicted in Figure 1.3.
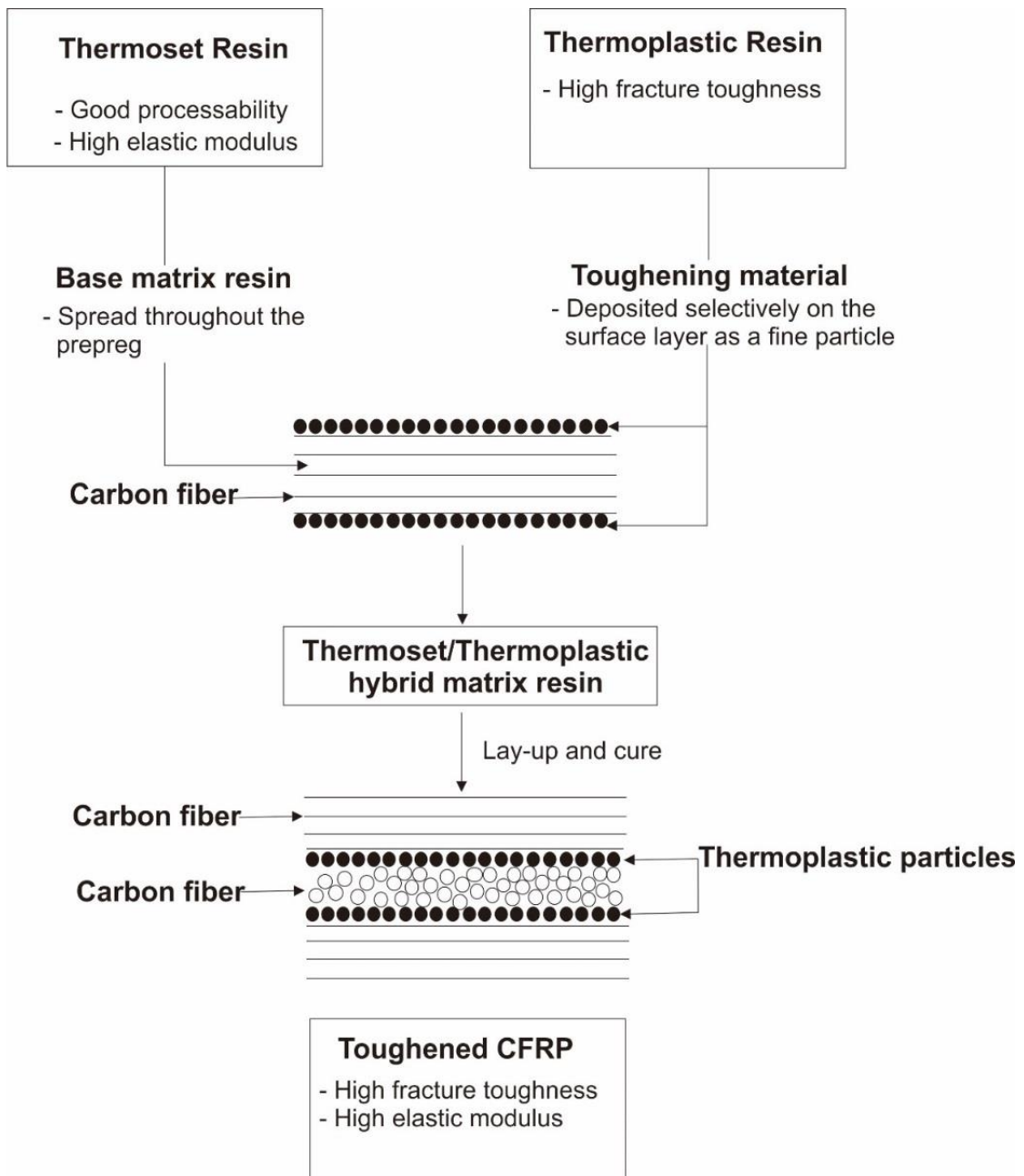
Figure 1.2: CFRP toughened with interlayer prepreg. Reproduced based on Odagiri et al. [8]
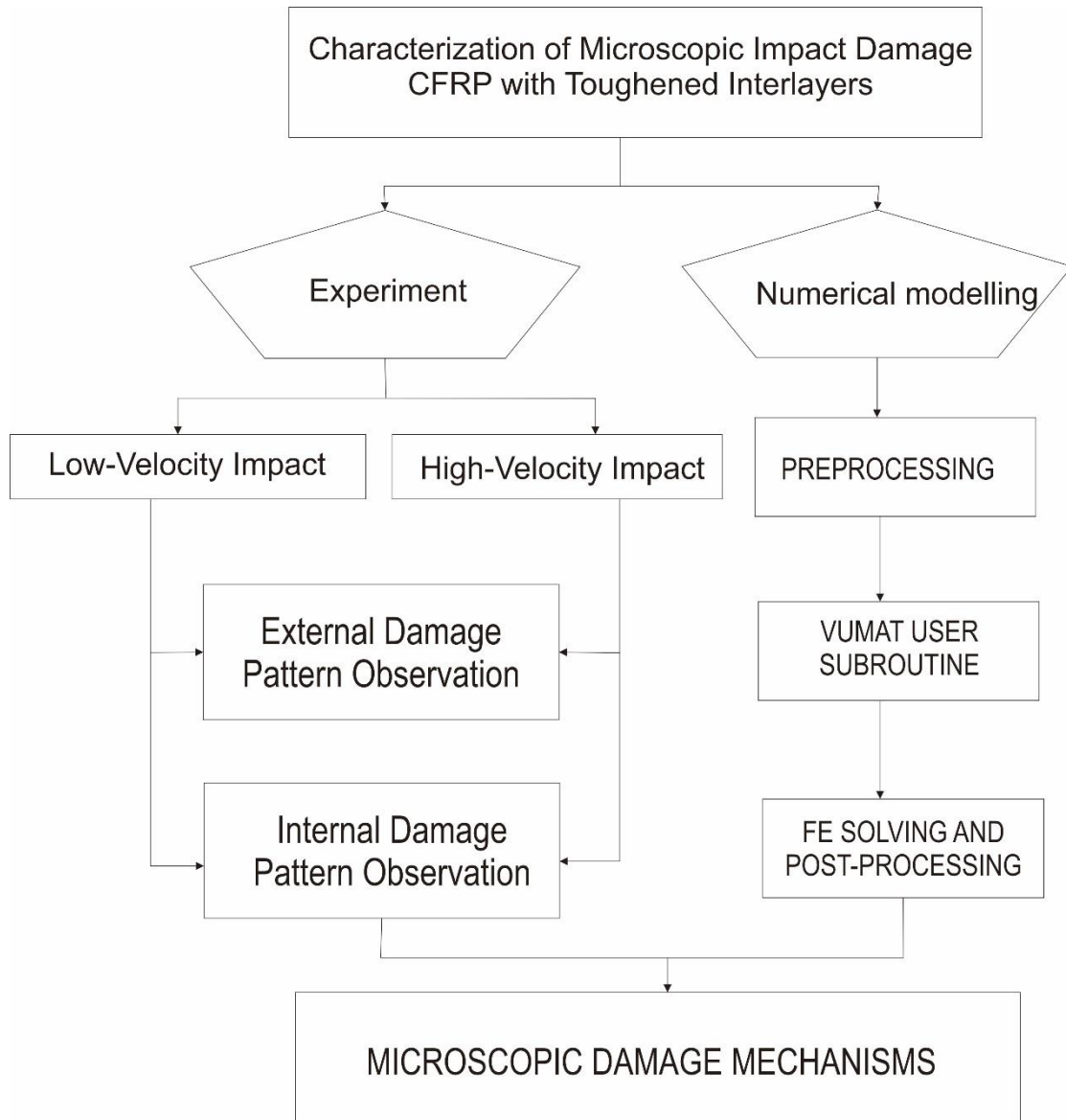
Figure 1.3: Overall research methodology.

1.3   Objective of Research

The objectives of this study are as follows:

1.   To characterize the microscopic damage mechanisms of CFRP with toughened

         interlayers when subjected to low- and high-velocity impacts.

2.   To develop numerical model of microscopic damage mechanisms of CFRP

         laminate with toughened interlayers when subjected to low-velocity impact.

3.   To compare the damage mechanisms of CFRP laminate with toughened

         interlayers between experiment and numerical modelling.

1.4   Outline of Thesis

This thesis comprises of six chapters as depicted in Figure 1.4. Firstly, Chapter One

outlines the background, problem statement and objectives of the research. Then, the

experimental setup is elucidated in Chapter Two. It describes the material preparation,

low- and high-velocity impacts testing apparatus as well as equipment used to observe

the damage after the impact. In Chapter Three, numerical modelling is described in detail

such as constitutive modelling of the laminate, failure criterion, delamination modelling

as well finite element modelling of the laminate. Chapter Four discusses the

characterization of microscopic damage of the laminate when subjected to low- and high-

velocity impacts. It explains the comparison observed in low- and high-velocity impacts as well as the different between toughened and untoughened laminate. Meanwhile, numerical modelling and experimental characterization of impact damage due to low-velocity impact are compared and discussed in Chapter Five. Lastly, general conclusion of this research is concluded in Chapter Six.
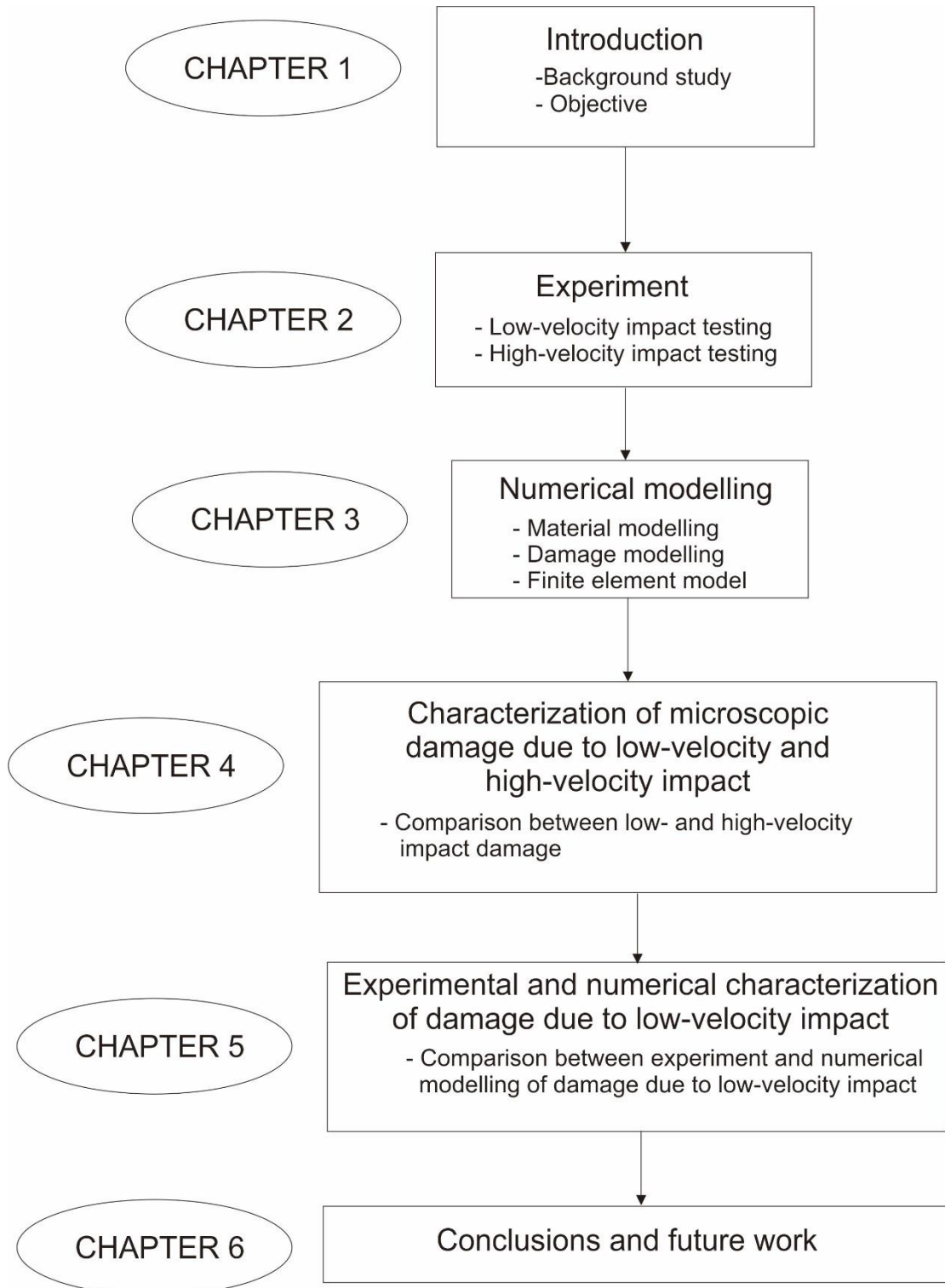
Figure 1.4: Outline of thesis.

CHAPTER 2: EXPERIMENT

2.1   Introduction

In this chapter, the experimental procedure is discussed in detail. Firstly, the material preparation is explained. After that, the experimental setup for both low-velocity and high-velocity impacts is described. The explanation includes the type of impactor, fixture and the equipment used. Finally, the damage observation method is elaborated especially with regard to the equipment used in this study.

2.2   Material Preparation

The material used in this study was T800S/3900-2B manufactured by Toray Industries Inc. It is a type of CFRP laminate toughened with the interlayers. The fiber strength of this material is about 10% higher than that of T800H/#3900-2. The stacking sequence was cross-ply lamination $[0^0/90^0]_{2S}$. Hereafter, the top and bottom plies are denoted as 0° plies. The total thickness of a cured laminate was 1.6 mm. The laminates were cut into square specimens of 55 mm wide and long by using diamond saw cutter equipped with diamond blade. Figure 2.1 depicts the schematic diagram of the specimen, whereas Figure 2.2 depicts the diamond saw cutter.
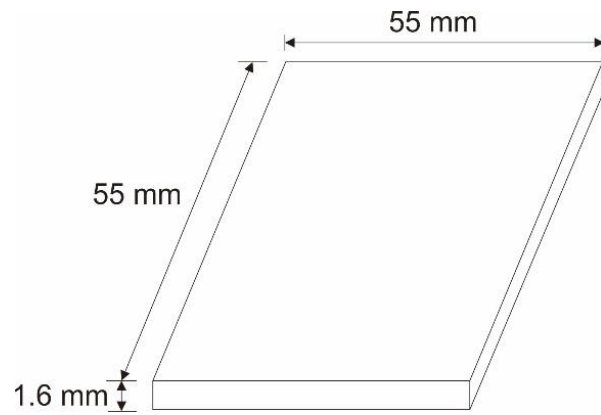
Figure 2.1: Schematic diagram of the specimen.

Figure 2.2: Diamond saw cutter.

Figure 2.3 presents the fixture jig supporting the specimen used in the low- and high-velocity impact tests. The target specimen was rigidly fixed along its four sides by a square frame with inner width of 50 mm. Hence, this support allows bending deformation of the target during both impact loads.

2.3   Low-Velocity Impact Testing Apparatus

Low-velocity impact test was conducted by using a guided drop-weight test jig illustrated in Figure 2.4. The impactor consists of a 15 mm diameter circular rod and a 1.5 mm diameter circular rod with the hemispherical tip whose diameter is the same as the projectile diameter for high-velocity impact test. The mass of impactors used was 62 g (Figure 2.5), 70.4 g (Figure 2.6) and 150 g (Figure 2.5). The impactor with a mass of 150 g is realized by screwing the additional mass to the impactor with a mass of 62 g. During the experiment, the impactor was suspended by a cable at a predetermined height to be dropped by free fall. The stopper was inserted to prevent the impactor from multiple impacts onto the specimen.

The drop height H in the low-speed impact test was predetermined from the kinetic energy E_{impact} of the projectile in the high-velocity impact test as follows:

$$H = \frac{E_{\text{impact}}}{Mg} \qquad (2.1)$$

with

$$E_{\text{impact}} = \frac{1}{2}mv^2 = MgH \qquad (2.2)$$

where M is mass of the low-velocity impactor, g is gravitational acceleration, and m and

v are mass and velocity of the high-velocity projectile, respectively. As mentioned above, the supporting conditions of the specimens, diameter of the projectile and the tip of impactor, and incident energy, which is variable, are the same in both impact tests.

(a)

(b)
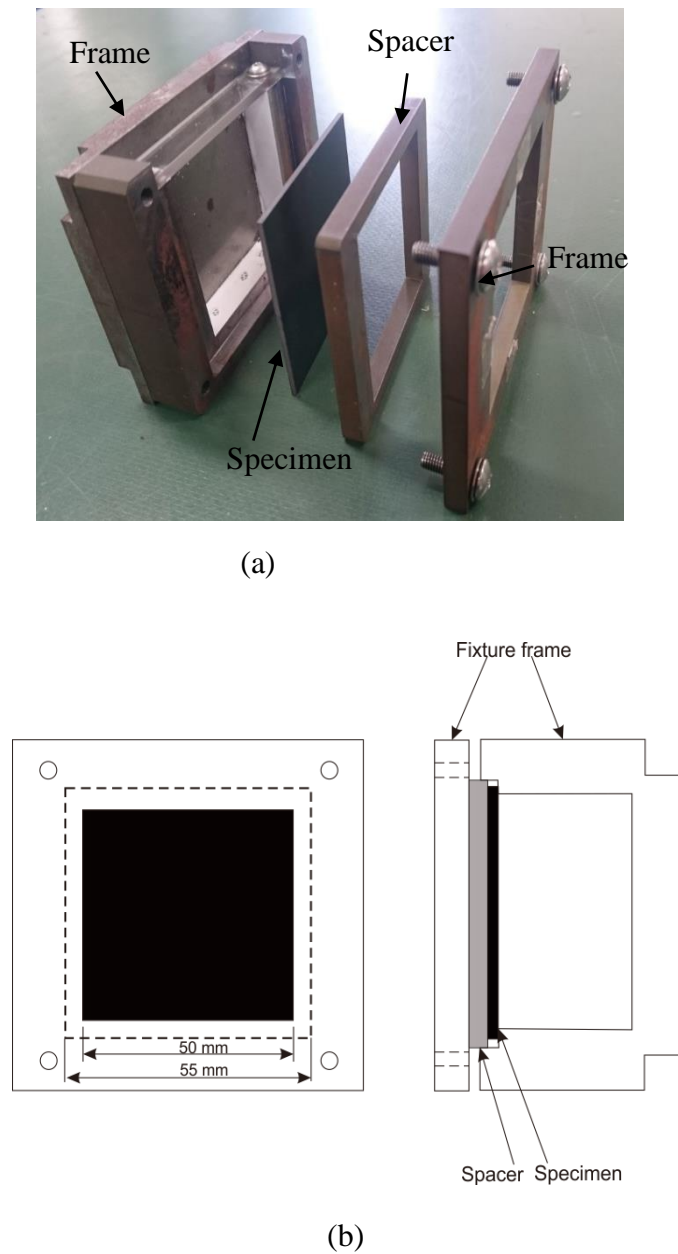
Figure 2.3: (a) Fixture jig for low- and high-velocity impact tests and (b) detail illustration of the fixture [65].
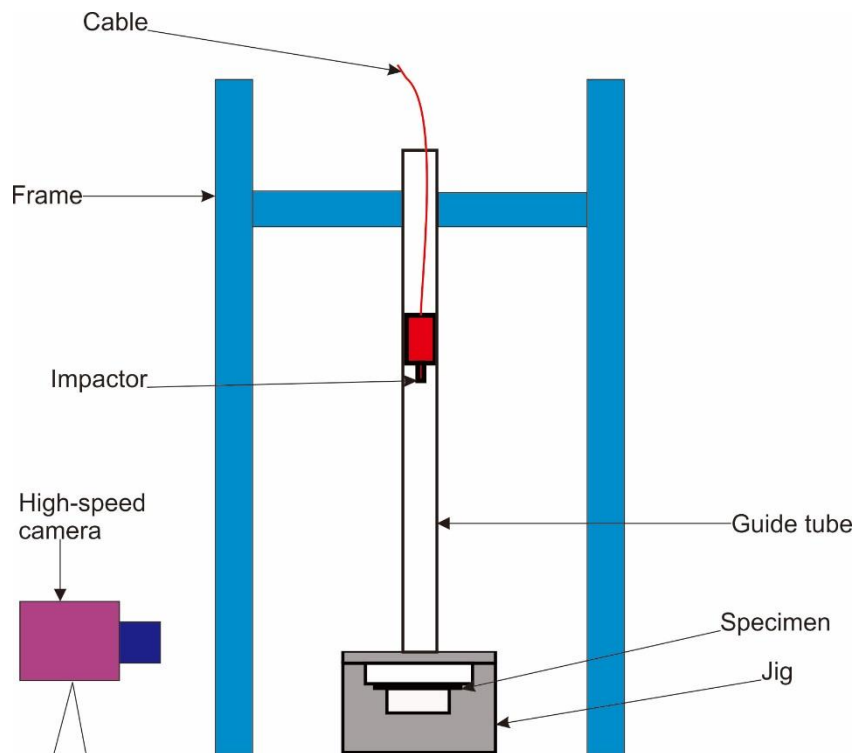
Figure 2.4: Schematic diagram of drop-weight test jig for low-velocity impact test [65].
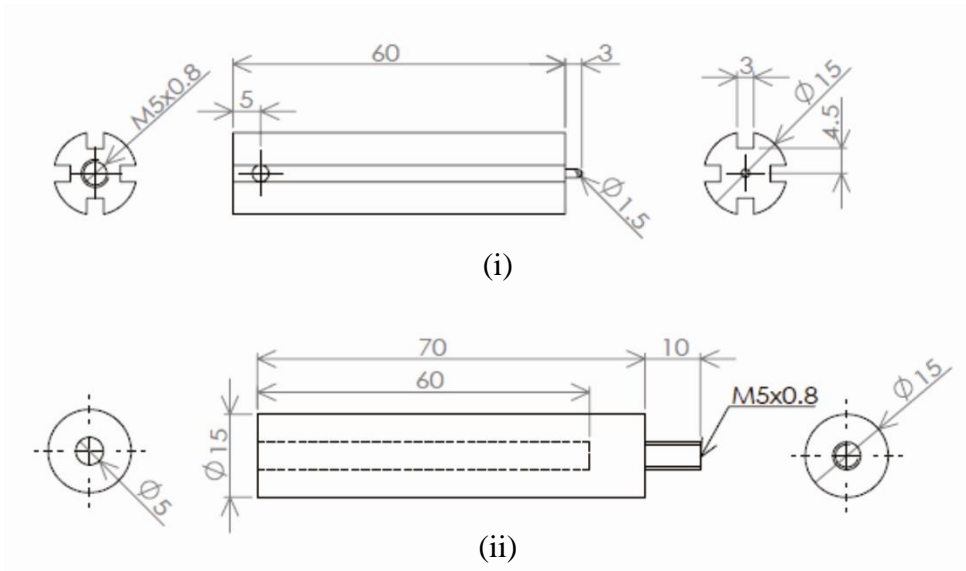
Figure 2.5: Illustration of (i) the impactor (62 g) and (ii) the additional mass (unit: mm) [65].
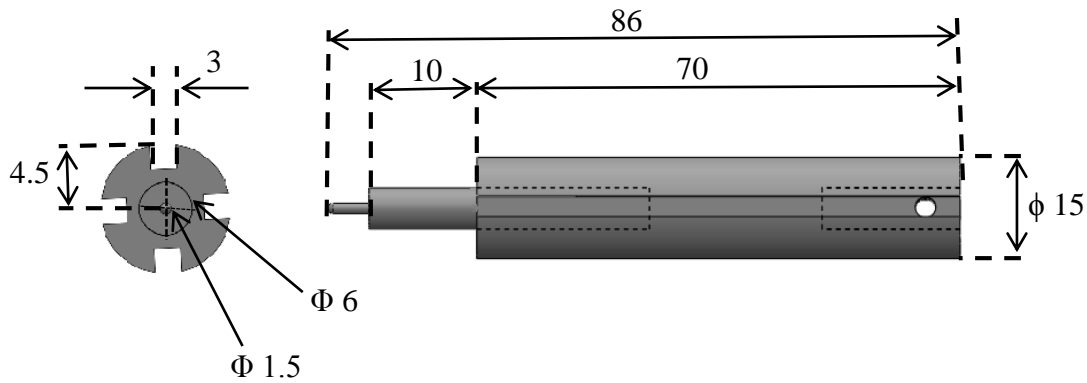
Figure 2.6: Illustration of the impactor (70.4 g) (unit: mm) [65].

The rebound height of the impactor and the deflection of the specimen were measured

with the aid of a high-speed camera, which took a movie during the impact test. The frame

rate was set 100000 fps and the deformation of the laminate was measured by using image

analysis software, Cine Viewer Application CV 2.5.

2.4   High-Velocity Impact Testing Apparatus

Figure 2.7 illustrates a high-velocity impact testing machine (Maruwa Electronic

Inc.) used in the experiment. The machine consists of a control unit for the power source

and a chamber in which a projectile is fired at a target as well as a speed detector

connected with a data logger. Steel balls with a diameter of 1.5 mm were used as

projectiles. The projectile was set in a sabot and accelerated at high-temperature and high-

pressure metal plasma. The metal plasma was generated by melting and evaporating an

aluminum foil subjected to high-voltage pulse current. The impact speed was approximately controlled by adjusting the applied voltage and precisely calculated from the period of time during which the projectile travels the prescribed distance (300 mm) in the speed detector. The velocity can be varied in the range of 40 m/s to 1500 m/s. When firing, the sabot was stopped at the opening of the gun and only the projectile was shot by inertia.
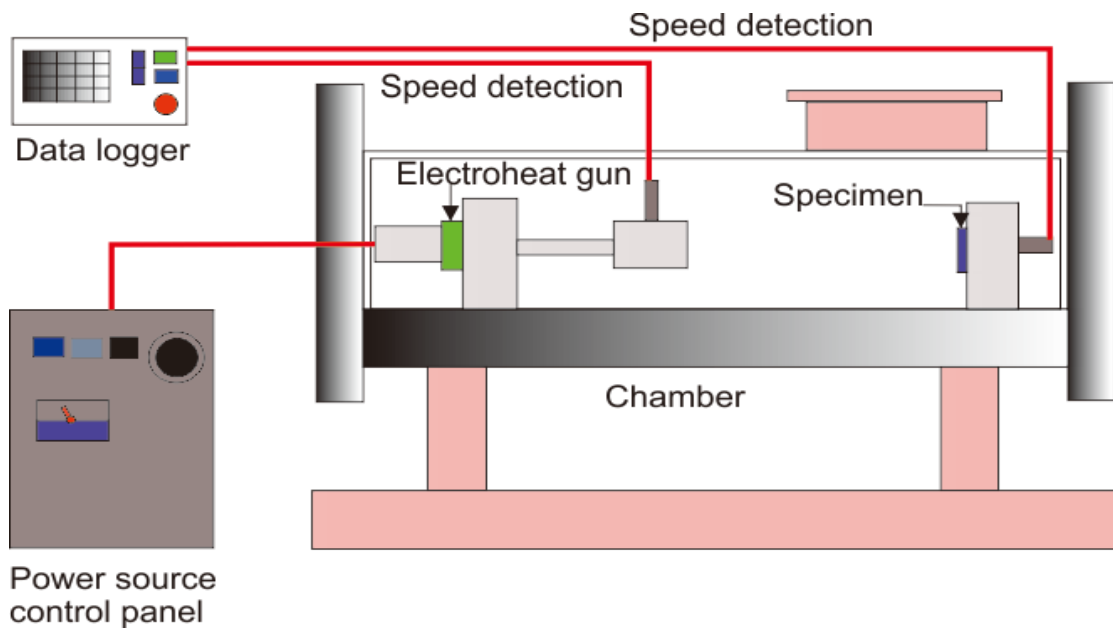
Figure 2.7: Schematic diagram of high-velocity impact testing machine [65].

2.5   Damage Observation Method

After the impact test, the damage on the specimen surface was observed by using stereoscopic microscope (OLYMPUS, SZX9) as depicted in Figure 2.8. Then, the internal

damage was quantitatively evaluated using soft X-ray radiography (SOFTEX M100) as

depicted in Figure 2.9. Moreover, several specimens were cut for detail observation of the

microscopic damage state on the cross-sections beneath the impact point. The observation

was made by using optical microscope (OLYMPUS, BX60M) as depicted in Figure 2.10.

Figure 2.8: Stereoscopic microscope.

Figure 2.9: Soft X-ray radiography.

Figure 2.10: Optical microscope.

CHAPTER 3: NUMERICAL MODELLING

3.1   Introduction

This chapter describes the numerical modelling employed in this study. The modelling is applied on a commercial FEA software namely, ABAQUS/Explicit. Firstly, the constitutive modelling of CFRP and the interlayer is described. After that, base ply failure criterion and delamination modelling are elucidated. Lastly, finite element model is explained. The overall modelling process in ABAQUS/Explicit is depicted in Figure 3.1.

3.2   Constitutive Modelling

For the purpose of this study, the laminate was modelled as bilayer plies consisting fiber layer (base ply) and the interlayer as a toughening agent. The base ply layer was modelled as an orthotropic elasticity whereas, the interlayer as an isotropic perfect elasto-plastic material. The base ply was defined by the nine independent elastic stiffness parameters. The stress-strain relations are of the form [29]:

$$\sigma = D\varepsilon \tag{3.1}$$

and in matrix form:

$$
\begin{Bmatrix} \sigma_{11} \\ \sigma_{22} \\ \sigma_{33} \\ \sigma_{12} \\ \sigma_{13} \\ \sigma_{23} \end{Bmatrix} = \begin{pmatrix} D_{1111} & D_{1122} & D_{1133} & 0 & 0 & 0 \\ & D_{2222} & D_{2233} & 0 & 0 & 0 \\ & & D_{3333} & 0 & 0 & 0 \\ & \text{\emph{sym}} & & D_{1212} & 0 & 0 \\ & & & & D_{1313} & 0 \\ & & & & & D_{2323} \end{pmatrix} \begin{Bmatrix} \varepsilon_{11} \\ \varepsilon_{22} \\ \varepsilon_{33} \\ \gamma_{12} \\ \gamma_{13} \\ \gamma_{23} \end{Bmatrix}
\tag{3.2}
$$

with

$$D_{1111} = E_1(1 - \nu_{23}\nu_{32})\Upsilon \tag{3.3}$$

$$D_{2222} = E_2(1 - \nu_{13}\nu_{31})\Upsilon \tag{3.4}$$

$$D_{3333} = E_3(1 - \nu_{12}\nu_{21})\Upsilon \tag{3.5}$$

$$D_{1122} = E_1(\nu_{21} + \nu_{31}\nu_{23})\Upsilon \tag{3.6}$$

$$D_{1133} = E_1(\nu_{31} + \nu_{21}\nu_{32})\Upsilon \tag{3.7}$$

$$D_{2233} = E_2(\nu_{32} + \nu_{12}\nu_{31})\Upsilon \tag{3.8}$$

$$D_{1212} = G_{12} \tag{3.9}$$

$$D_{1313} = G_{13} \tag{3.10}$$

$$D_{2323} = G_{23} \tag{3.11}$$

where

$$\Upsilon = \frac{1}{1 - \nu_{12}\nu_{21} - \nu_{23}\nu_{32} - \nu_{31}\nu_{13} - 2\nu_{21}\nu_{32}\nu_{13}} \tag{3.12}$$

On the other hand, the stress-strain relationship of the interlayer is given by:

$$
\begin{Bmatrix} \varepsilon_{11} \\ \varepsilon_{22} \\ \varepsilon_{33} \\ \gamma_{12} \\ \gamma_{13} \\ \gamma_{23} \end{Bmatrix} = \begin{pmatrix} 1/E & -v/E & -v/E & 0 & 0 & 0 \\ -v/E & 1/E & -v/E & 0 & 0 & 0 \\ -v/E & -v/E & 1/E & 0 & 0 & 0 \\ 0 & 0 & 0 & 1/G & 0 & 0 \\ 0 & 0 & 0 & 0 & 1/G & 0 \\ 0 & 0 & 0 & 0 & 0 & 1/G \end{pmatrix} \begin{Bmatrix} \sigma_{11} \\ \sigma_{22} \\ \sigma_{33} \\ \sigma_{12} \\ \sigma_{13} \\ \sigma_{23} \end{Bmatrix} \qquad (3.13)
$$

The material properties for both base ply and the interlayer is summarized in Table 3.1.

Table 3.1: Material properties of CFRP with toughened interlayers.

	Base ply [30]		Interlayer
Young's modulus E (GPa)	Longitudinal E_1	151	4.6 [30]
	Transverse $E_2 = E_3$	9.16	
Shear modulus G (GPa)	$G_{12}=G_{13}$	4.62	1.6 [30]
	G_{23}	2.55	
Poisson's ratio v	$v_{12} = v_{13}$	0.302	0.44 [30]
	v_{23}	0.589	
Yield strength (MPa)			64 [31]
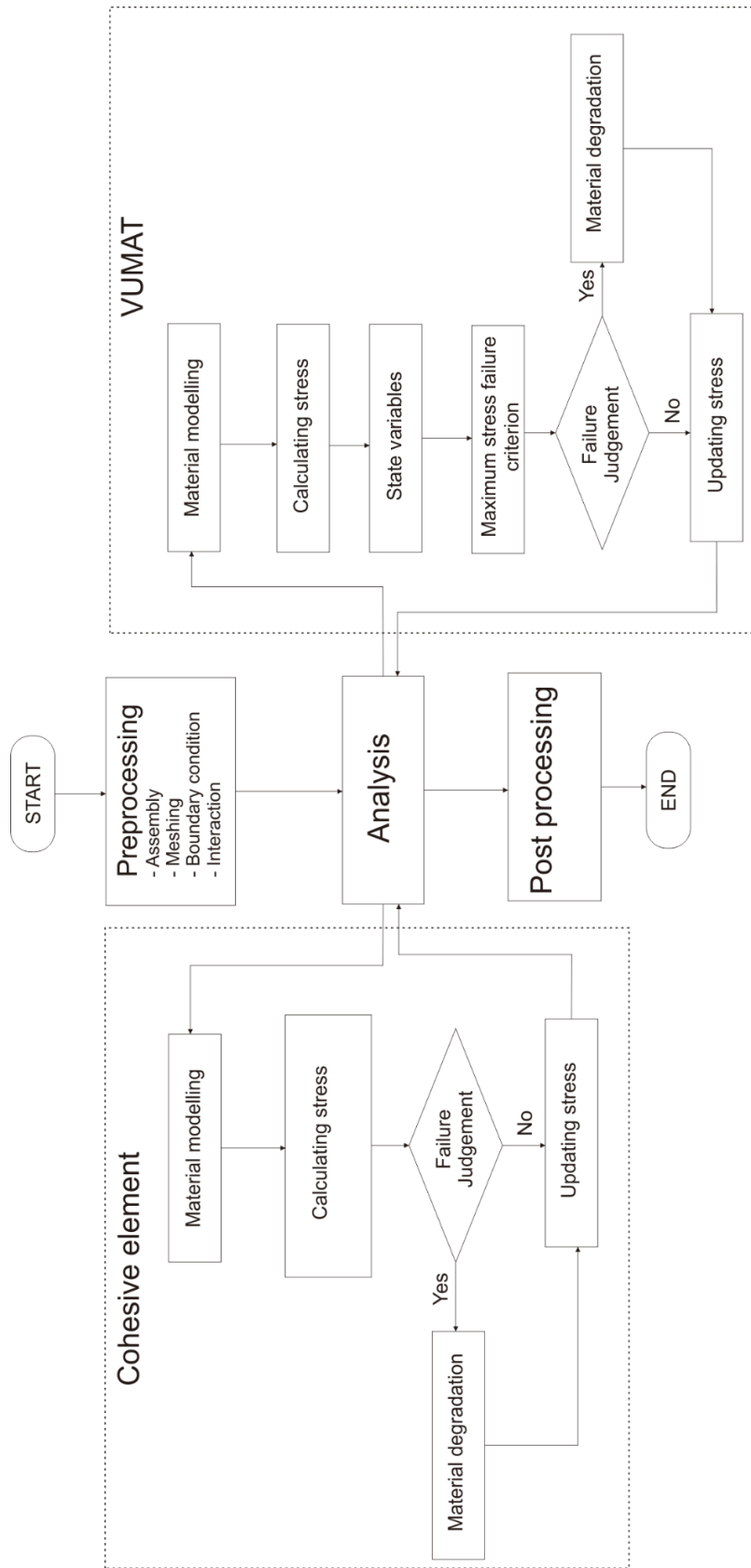
Figure 3.1: Flow chart of ABAQUS/Explicit numerical simulation.

3.3   Base Ply Failure Criterion

The maximum stress criterion was employed as a failure criterion for the base ply.

A user subroutine program (VUMAT) was incorporated in ABAQUS/Explicit software

to perform failure analysis by expressing the tensile failure in the fiber and transverse

directions, compressive failure in fiber direction and in addition to in-plane and out-of-

plane shear failure. Table 3.2 lists the type of failure applied in the modelling. The failure

is satisfied if: (3.14)

$$\frac{\sigma_{ij}}{S_{ij}} \geq 1$$

where σ_{ij} is stress and S_{ij} strength. The strength of the base ply is summarized in Table

3.3. When the element was failed, the stiffness and stresses of the failed element were

degraded, considering the damage and stress transfer mechanism by following this

equation [32]:

$$E'_{ij} = k_{ij}E_{ij} \qquad (3.15)$$

where E'_{ij} is the degraded elastic modulus, E_{ij} elastic modulus and k_{ij} is a

degradation rule or knockdown factor as listed in the Table 3.4. When one of the failure

criteria was satisfied, the stress components related to the damage mode were set to zero,

and the relevant stiffness was updated to the degraded value. The degradation factors

should be zero at a crack surface, but nonzero values were applied considering stress

recovery in element and these values were fitted to the experiments [33].

In order to avoid non-realistic failure of the base plies at the vicinity of impact point, compressive failure in the transverse and through-the-thickness directions was not considered. On the other hand, no failure criterion was applied to the interlayers because they act as crack arrestors as described later.

Table 3.2: Failure criterion for the base ply.
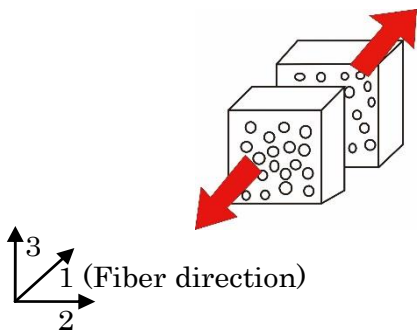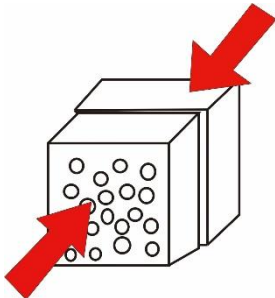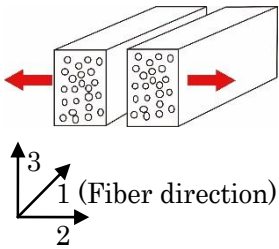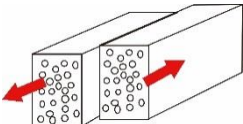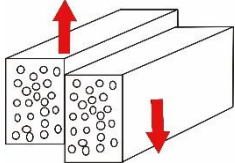
Fiber failure	
Tension (Longitudinal)	Compression (Longitudinal)
Matrix damage		
Tension (Transverse)	In-plane shear	Out-of-plane shear

Table 3.3: Strength of the base ply.

Direction of strength	Strength (MPa) [34]
Tensile strength in the fiber direction	3108
Compressive strength in the fiber direction	719.4
Tensile strength in the transverse direction	67
In-plane shear strength	100
Out-of-plane shear strength	100

Table 3.4: Degradation rule.

Failure mode	Knockdown factor, k_{ij}
Tensile (Longitudinal)	0.9
Compression (Longitudinal)	0.9
Tensile (Transverse)	1.0
In-plane shear	0.8
Out-of-plane shear	0.8

3.4   Delamination Modelling

The modeling of delamination was carried out based on the work by Camanho and

Davilla (2002) [35] and applied in ABAQUS/Explicit software [29]. The modelling was

applied to the interface element which was inserted between each ply. This interface

element is denoted as "cohesive element" in the software. The prediction of delamination

onset was based on stress failure criterion, whereas delamination propagation was based

on fracture mechanics concept. As the name implies, damage initiation refers to the

beginning of degradation of the response of a material point. The process of degradation

begins when the stresses satisfy certain damage initiation criteria. Damage is assumed to initiate when a quadratic interaction function involving the nominal stress ratios reaches a value of one.

This stress failure criterion can be represented as [24]:

$$\left(\frac{\langle\sigma_n\rangle}{N}\right)^2 + \left(\frac{\sigma_s}{S}\right)^2 + \left(\frac{\sigma_t}{T}\right)^2 = 1 \tag{3.16}$$

where σ_n, σ_s and σ_t denote the traction stresses in normal, n and shear directions, s and t respectively. Meanwhile, N, S and T denote the interlaminar strength in normal and two shear directions respectively. Before the onset of delamination, the traction stresses can be calculated by using similar penalty stiffness of mode I, II and III, K and the separation/displacement, δ_i :

$$\tag{3.17}$$

$$\sigma_i = K\delta_i;\ i = n,\ s,\ t$$

The initial response of the cohesive element is assumed to be linear. However, once a damage initiation criterion is met, the material stiffness is gradually degraded in terms of a damage variable, d. This variable is defined as:

$$d = \frac{\delta_m^f(\delta_m^{max} - \delta_m^o)}{\delta_m^{max}(\delta_m^f - \delta_m^o)} \tag{3.18}$$

where δ_m^{max} refers to the maximum value of mixed-mode displacement attained during loading history, δ_m^f mixed-mode displacement at complete failure, δ_m^o mixed-mode displacement at damage initiation. Its value ranging from zero when the damage initiates

and one when complete delamination generated in cohesive element. A typical linear

relationship of traction-separation model for fracture modes I, II and III is depicted in the

Figure 3.2. The initial response of the cohesive element is linear elastic represented by

stiffness up to the interlaminar shear strength. Once it reaches the strength, the stiffness

will degrade based on damage variable, d and the damage will be initiated.
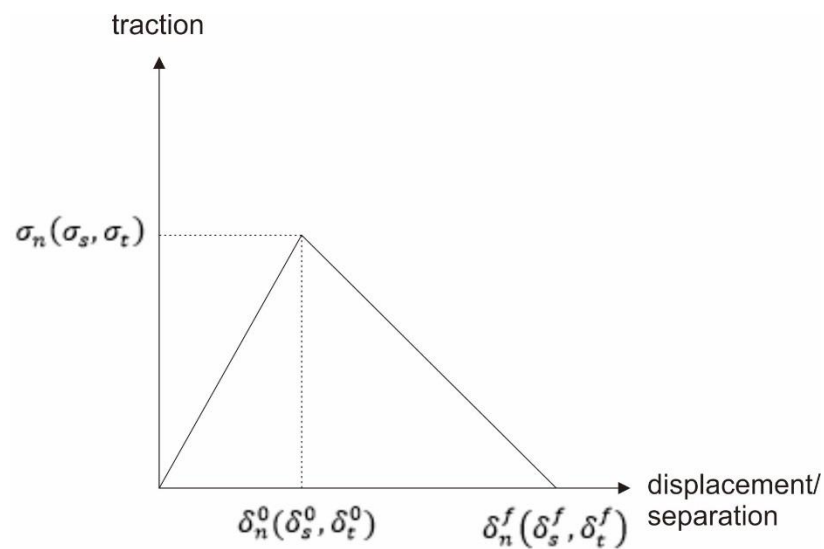
Figure 3.2: Typical linear relationship of traction-separation response for mixed-
mode fracture.

The failure criterion to calculate delamination propagation was based on energy

release rates under mixed-mode loading; mode I, II and III. The damage evolution can be

defined based on the energy that is dissipated as a result of the damage process, also called

the fracture energy. The fracture energy is equal to the area under the traction-separation

curve as depicted in Figure 3.3. The Benzeggagh-Kenane fracture criterion is particularly

useful when the fracture energies during deformation purely along the first and the second

shear directions are the same [36]. The damage is assumed to grow for a mixed mode

fracture when the energy release rate is equal or greater than critical energy release rate,

G^C;

$$G^C = G_{IC} + (G_{IIC} - G_{IC})\left\{\frac{G_{shear}}{G_T}\right\}^{\eta} \tag{3.19}$$

where $G_{shear} = G_{II} + G_{III}$ is an energy release rate for mixed-mode shear loading,

$G_T = G_I + G_{shear}$ total energy release rate and η a parameter obtained in the mixed-

mode bending experiment.
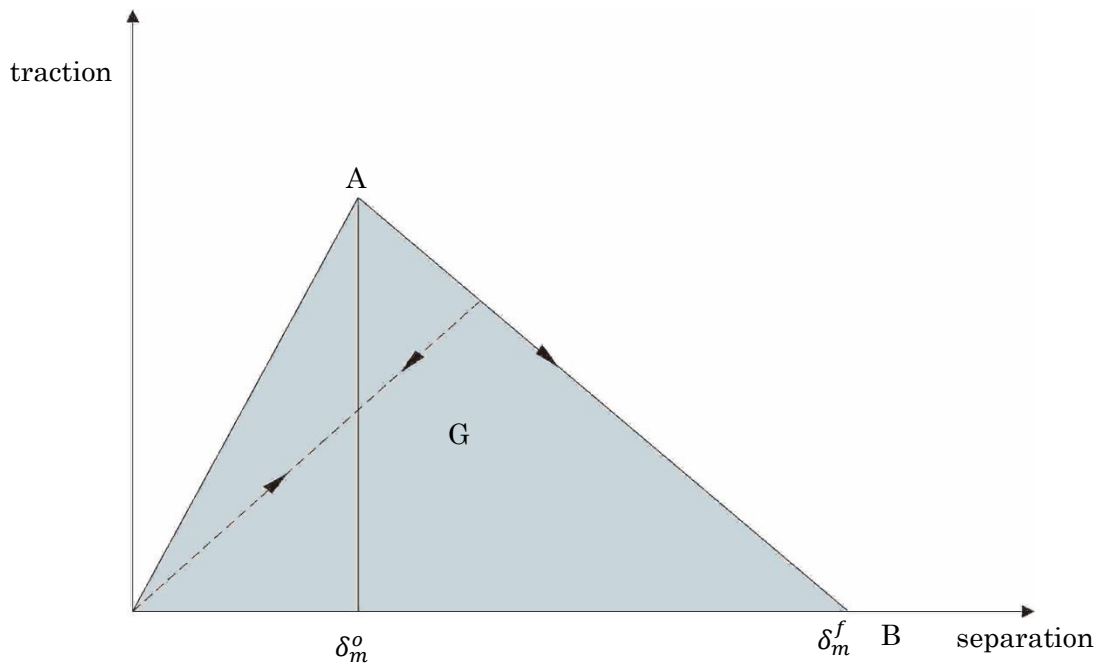
Figure 3.3: Linear damage evolution.

The properties of the cohesive elements to simulate the delamination are given in Table 3.5.

Table 3.5: Properties of cohesive elements.

Properties	Interlaminar delamination [34]	Intralaminar delamination [6]
In-plane tensile strength (MPa) N	80	60
In-plane and out-of-plane shear strength S, T (MPa)	160	100
Mode I critical energy release rate, G_{IC} (J/m^2)	540	200
Modes II & III critical energy release rate, G_{IIC} & G_{IIIC} (J/m^2)	1640	500
η parameter [32]	1.5	1.5

3.5   Finite Element Model

A quarter model 13.75 mm square was adopted for symmetry (see Figure 3.4). The thickness of the base ply and the interlayer was 0.183 mm and 0.02 mm, respectively. 3D deformable solid body elements (C3D8R) were employed for both base plies and interlayers. In contrast, the impactor was assumed to be a rigid body with a hemispherical head whose diameter was 1.5 mm. The initial velocity was applied to the projectile to simulate the impact event. In addition, cohesive elements were introduced to express delamination generated between the base ply and the interlayer as well as inside the base plies as depicted in Figure 3.5. Hereafter, the former and the latter delaminations are

denoted as *interlaminar* and *intralaminar* ones, respectively. The total numbers of elements and nodes were 220,615 and 453,805, respectively.

On the other hand, in order to simulate the difference with and without intralaminar delamination, cohesive elements were removed inside the base ply as depicted in Figure 3.6.
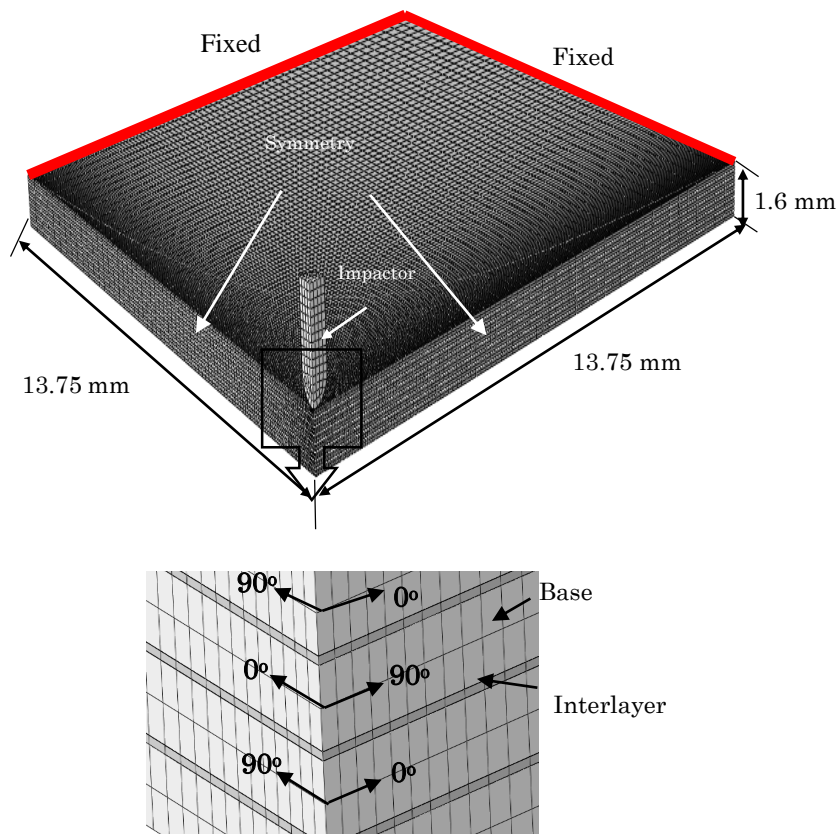
Figure 3.4: FEA model (units: mm) [66].
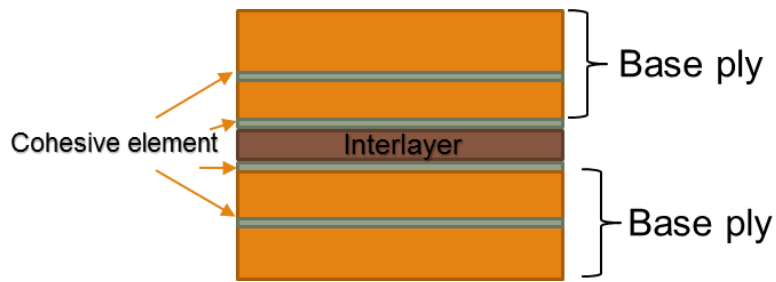
Figure 3.5: Insertion of cohesive elements in the FEA model at the interfaces of interlayer and base ply as well as within base ply [66].
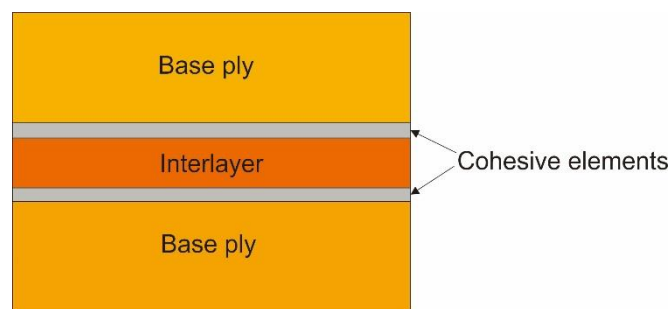
Figure 3.6: Insertion of cohesive elements in the FEA model at the interfaces of interlayer and base ply only.

3.5.1   Interaction and Contact Modelling

General contact algorithm in ABAQUS/Explicit was used in this study for contact modelling. The contact includes contact between impactor and the laminate as well as internally adjacent plies of the laminate. This contact algorithm has only a few restrictions compare to contact pair algorithm. Furthermore, this contact allows the use of element based surface to model element erosion during the analysis. General contact algorithm also creates contact force based on the penalty enforcement contact method. The friction

coefficient is used to account for shear stress of the surface traction with contact pressure.

In general, the friction coefficient is determine by material stiffness and the roughness of the surface. There is a suggestion from previous study to use 0.2 as friction coefficient for $0°/0°$ laminate and 0.8 for the interface between adjacent $90°$ plies [24]. In the current study, an average friction coefficient of 0.5 was chosen between the $0°/90°$ interface of cross ply laminate [32].

Another contact modelling used was tie constraint method. The purpose of this contact method is to tie cohesive element surface to solid element surface to ensure the continuity between these two types of elements. In this respect, the solid element was regarded as master surface, whereas the cohesive element as slave surface

3.5.2   Boundary Conditions

Based on the experimental setup, the laminate was clamped at it edges (Figure 2.3). Thus, in the modelling, the edges of the laminate were fixed in all axes ($x = 0$, $y = 0$, $z = 0$). Since the laminate was a quarter model, symmetrical boundary condition in x- and y-axis were applied at the cross section of the

laminate (Figure 3.4). In addition, tie constraint was applied between cohesive

elements and solid elements of the laminate. On the other hand, the impactor was

fixed in x- and y-axis and allowed movement in z-axis only. Since the impactor

was modelled as a rigid body, the reference point was assigned at the nose of

impactor and the value of velocity in z-axis was assigned at the reference point.

CHAPTER 4: CHARACTERIZATION OF MCROSCOPIC DAMAGE DUE TO LOW-VELOCITY AND HIGH-VELOCITY IMPACT IN CFRP WITH TOUGHENED INTERLAYERS

4.1   Introduction

Carbon fiber reinforced plastics (CFRPs) have been used in many applications because of high specific strength and specific modulus as well as good fatigue properties. For example, CFRPs have been used in primary structures such as a fuselage, wing and turbofan engine of recent civil aircraft. In general, CFRPs are vulnerable to out-of-plane impact load, which may cause internal and external damage, leading to reduction of the strength and the stiffness of CFRP. The damage due to low-velocity impact like tool-drop can be classified into clearly visible impact damage (CVID) or barely visible impact damage (BVID). In the latter case, although only the small dent is created on the laminate surface, large-scale damage including matrix cracking and delamination is often generated inside the laminate. In contrast, high-velocity impact produces clear evidence such as a crater on the surface in addition to more catastrophic failure than low-velocity impact.

A lot of work has been conducted on low- and high-velocity impacts damage. Abrate [37][38][39] made an extensive review on impact dynamics, damage modes, failure

criteria and residual properties for low-velocity impact as well as ballistic limit and ballistic impact damage for various kinds of composites. Regarding high-velocity impact, Goldsmith et al. [40] carried out both quasi-static and ballistic impact tests for CFRP. They suggested that the damage process includes global plate deflection, fiber failure, crack propagation, petaling, delamination, hole enlargement and friction. Lopez-Puente et al. [41] investigated quasi-isotropic and woven laminates subjected to high-velocity impact and their dependency on temperature. The delaminated area of the quasi-isotropic laminates is greater than the woven laminates for any given impact velocity and temperature. Tanabe et al. [42] studied the fracture behavior of CFRP using different types of carbon fiber and they concluded that the mechanical properties at rear layers contribute to improve the energy absorption. Hazell et al. [43] studied damage mechanism of CFRP when subjected to normal and oblique impact at a high velocity.

On the other hand, in terms of low-velocity impact, Mitrevski et al. [44] studied the effect of various projectile shapes, namely, hemispherical, conical and ogival. Conical and ogival impactors generate permanent indentation and penetration whereas a hemispherical impactor produces BVID. The characteristics of low-velocity impact damage and its residual tensile strength were investigated by Wang et al. [17]. They observed that two different tensile damage modes are produced after different impact

energies. Heimbs et al. [45] studied impact load coupled with a pre-stress condition and found that delamination is a major energy absorption mechanism.

In order to improve the out-of-plane mechanical properties of composite laminates, several methods have been developed, for example, stitching [46][47][48], matrix toughening [49][50], critical ply termination and edge cap reinforcement [51]. One of the technique to increase the interlaminar fracture toughness is to introduce toughened interlayers including toughening particles or nanofiber. Several studies on low-speed impact for such CFRP laminates have been performed by Ito et al. [52], Bull et al. [20], and Xu et al. [22]. Morita et al. [11][12] studied the low-velocity and high-velocity (up to 130 m/s) impact damage for three types of material systems, carbon fiber/polyether-ether-ketone (CF/PEEK), CF/polyether-ether-ketone (CF/PEEK) with interlayers and CF/epoxy with toughened interlayers (T800H/#3900-2, Toray Industries Inc.). They found that both low- and high-velocity impacts damage primarily consists of matrix cracking and delamination. Consequently, the failure modes for both impact tests become similar while the damage area is larger in high-velocity impact. Moreover, they focused on the final damage state and discussed the relationship between damage area and the impact energy.

When a fan blade-out event in a turbofan engine is considered, a composite fan case

needs to bear the impact with a velocity near and/or higher than the sound velocity. Recently, Yashiro et al. [33][53][54] have studied the high-velocity (up to 900 m/s) impact damage process of CFRP laminates. They have experimentally characterized microscopic damage state and numerically reproduced the damage process using a smoothed-particle hydrodynamics (SPH) method. However, the difference of microscopic damage process between high- and low-velocity impact tests has not thoroughly been investigated for CFRP with toughened interlayers. In addition, the effect of toughened interlayers on low- and high-velocity impacts damage is not fully understood yet because the delamination behavior depends on the loading mode.

This chapter aims at characterizing microscopic damage in CFRP cross-ply laminates with toughened interlayers. The microscopic damage state is compared in detail between low- and high-velocity impact tests. Both impact tests were performed under the same conditions except for impact velocity. Since the present study simulates damage due to the fan blade-out event by broken fan blade pieces, the tip diameter of impactor and projectile is small. Instead, the impact damage was observed for a wide range of velocity while the incident energy range is relatively small. As a result, the degree of damage varies widely from BVID to perforation with fiber breakage. In addition, the effect of interlayers on impact damage is elucidated by means of microscopic damage observation,

being focused on crack propagation in the vicinity of the interlayers.

4.2 Low-Velocity Impact

Figure 4.1 depicts the damage generated on the front surface of the laminate at specified impact velocities and energies. A specimen with the highest velocity and energy (Figure 4.1(d)) is fully penetrated by the impactor. All the specimens except specimen 1 have a dent or a crater with two cracks propagating in the transverse (normal to the fiber) direction while any splitting cracks parallel to the fiber direction are not generated. In contrast, the splitting cracks as well as bulging area are observed on the back surface of the laminate as depicted in Figure 4.2. These cracks were generated only when the impact energy is the highest ($E = 2.92$ J).

Typical soft X-ray photographs of the laminates are presented in Figure 4.3. The delamination propagates chiefly in the fiber direction, while the delamination propagation in the transverse direction is limited. The laminates without full penetration (Figures 4.3(a) and 4.3(b)) exhibit a peanut-shape delamination while the delamination in the laminate with full penetration is in a galaxy-shape (Figure 4.3(c)).

Figure 4.4 shows optical micrographs of cross-sections of the specimens after low-velocity impact. The interlayers are observed as resin-rich layers between the base 0° and

90° plies. It should be noted that the fiber directions in the top and bottom plies are normal

to the photographs. Figure 4.4(a) depicts the cross-section of the specimen 1 for $v = 2.4$

m/s and $E = 0.18$ J. No internal damage is observed. Figure 4.4(b) depicts the damage

state beneath the impact point for $v = 4.9$ m/s and $E = 0.74$ J.

(a) Specimen 1; m = 62 g; v = 2.4 m/s; E = 0.18 J

(b) Specimen 2; m = 62 g; v = 4.9 m/s; E = 0.74 J

(c) Specimen 3; m = 62 g; v = 6.0 m/s; E = 1.13 J

(d) Specimen 4; m = 150 g; v = 6.0 m/s; E = 2.92 J
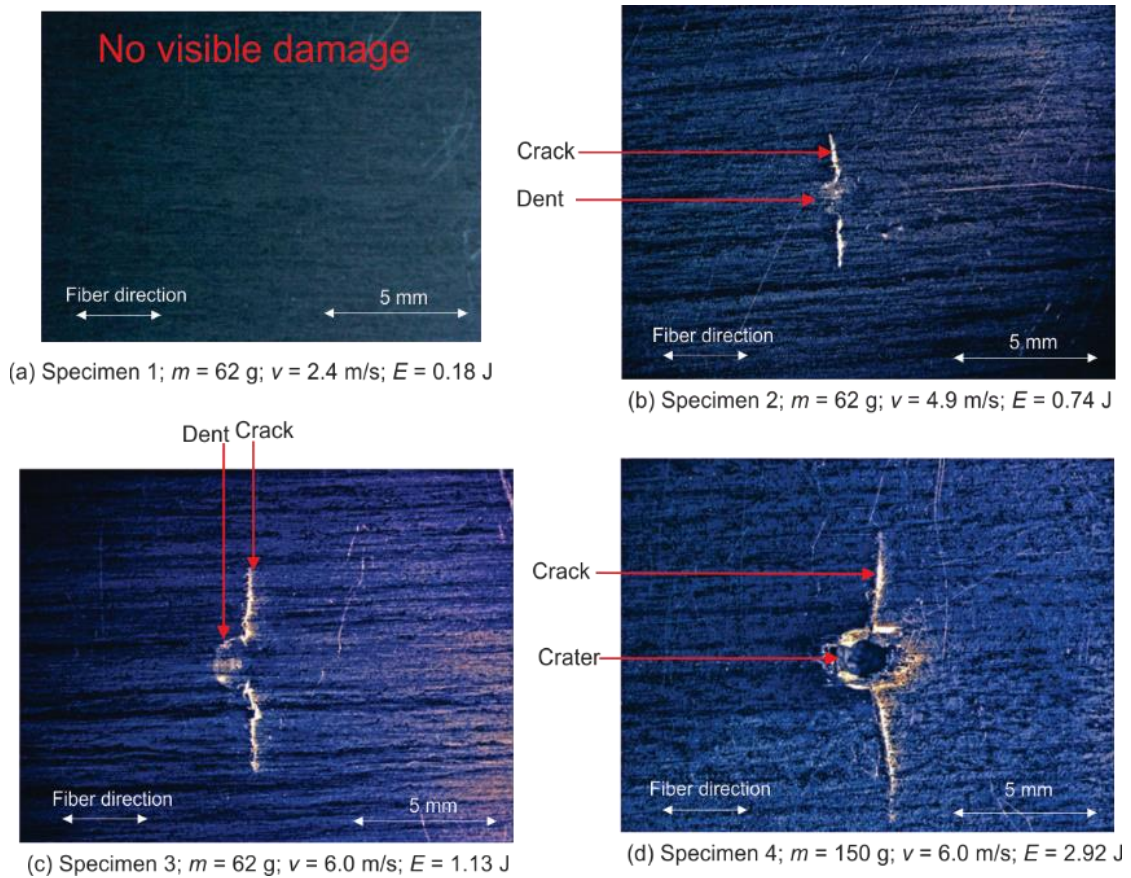
Figure 4.1: Damage on the front surface of the laminates after low-velocity impact
[65].

A dent, delamination and matrix cracks including bending cracks in the bottom ply

and cone cracks in the middle plies are generated. The matrix cracks in the top ply are

separated into two lateral cracks, one of which is delamination at the interface between

the top ply and the first interlayer (arrow A), and the other is the lateral crack in the top

ply (arrow B). Hereafter, this lateral crack is referred to as intralaminar delamination. Several bending cracks in the bottom ply is supposed to be due to global bending deformation during impact. Most of the matrix cracks stop at the interface between the base ply and the interlayer (arrow C). Figure 4.4(c) depicts the damage state for $v = 6.0$ m/s and $E = 1.13$ J. The damage state is similar to that in Figure 4.4(b) although slight permanent deformation is observed after impact.

Specimen 4; $m = 150$ g; $v = 6.0$ m/s; $E = 2.92$ J
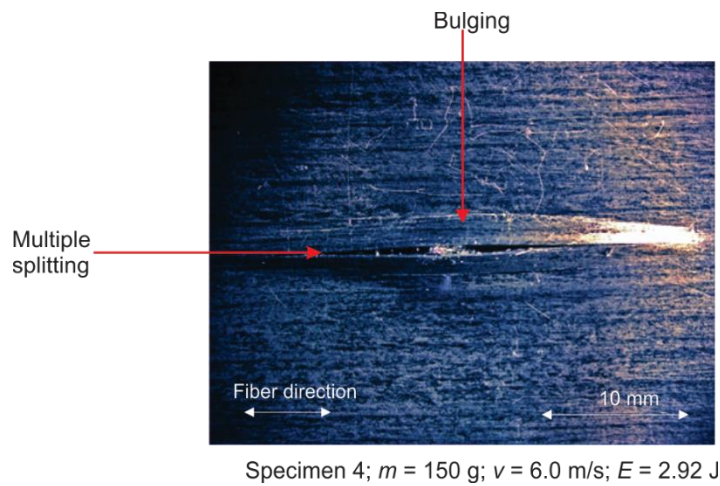
Figure 4.2: Damage on the back surface of the laminate after low-velocity impact [65].

(a) Specimen 2; $m = 62$ g; $v = 4.9$ m/s; $E = 0.74$ J

(b) Specimen 3; $m = 62$ g; $v = 6.0$ m/s; $E = 1.13$ J

(c) Specimen 4; $m = 150$ g; $v = 6.0$ m/s; $E = 2.92$ J

Figure 4.3: Soft X-ray photographs of the laminates after low-velocity impact [65].

54

Figure 4.4(d) presents the damage state for $v = 6.0$ m/s and $E = 2.92$ J. Although the

impact velocity in Figure 4.4(d) is the same as that in Figure 4.4(c), the impactor fully

penetrates through the specimen because impact energy is higher due to increasing mass.

The impact area on the top surface is no longer a dent but a crater with bulging and all

the plies including interlayers break in the penetration region. In the vicinity of the

penetration region, interlaminar delamination (arrows D) as well as matrix cracks (arrows

E) are generated. The bottom ply bends downward and some broken fibers peel off from

the laminate (see Figure 4.2). This damage state is quite different from the above two

conditions and rather similar to high-velocity impact damage state as will be shown later.

4.3   High-Velocity Impact

Figure 4.5 depicts the damage generated on the front and the back surfaces of the
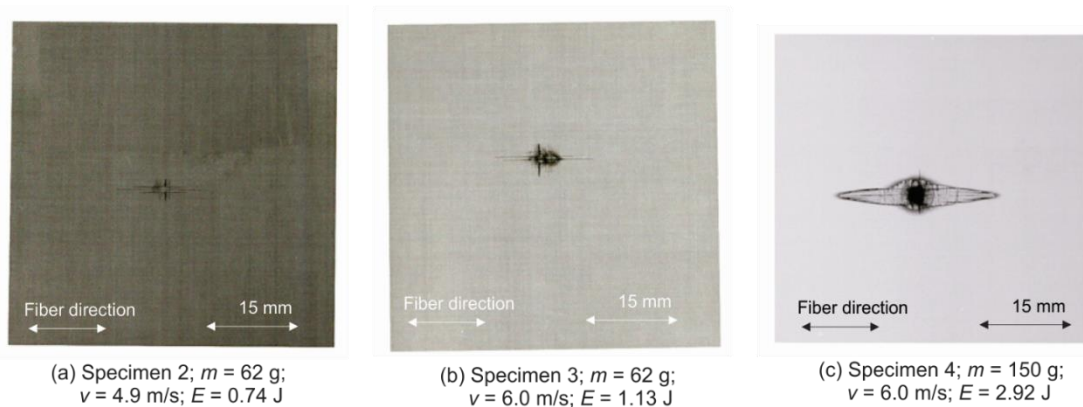
laminates after the high-velocity impact test. A crater and multiple splitting cracks

propagating in the fiber direction are observed for three impact velocities. It is found that

the length of the splitting cracks becomes longer as the impact velocity or energy

increases. The several broken fibers inside the crater peel off from the laminate. On the

other hand, the damage state on the back surface differs among the three velocities. At v

$=160$ m/s, the damage is barely visible on the back surface. A small bulge is generated at

$v = 327$ m/s whereas no cracking is observed. At $v = 651$ m/s, the laminate is fully

perforated by a projectile, and multiple splitting cracks with fiber breakage appear on the

back surface.
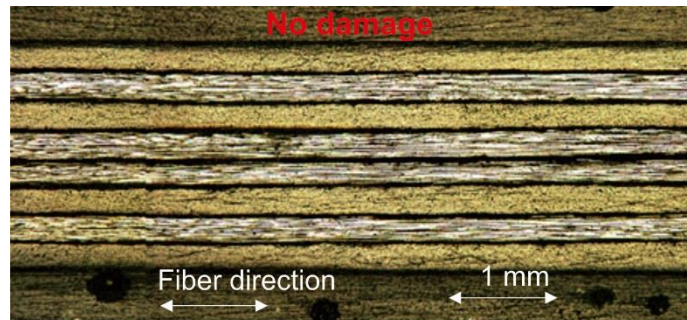
(a) Specimen 1; m = 62 g; v = 2.4 m/s; E = 0.18 J
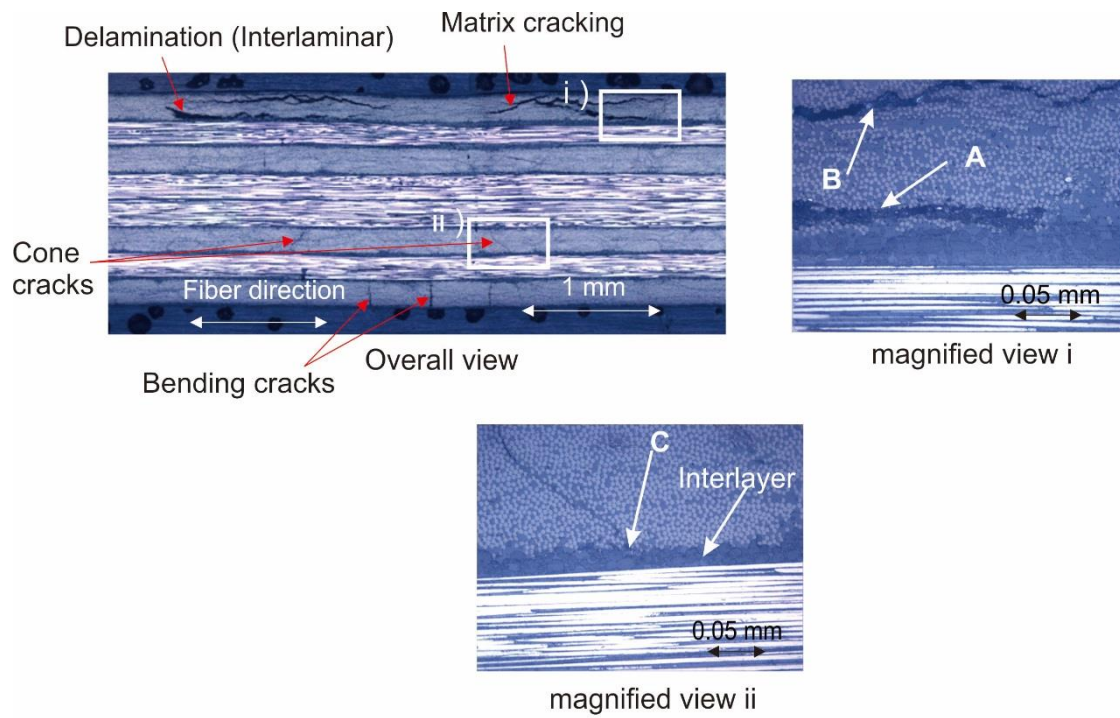
(b) Specimen 2; m = 62 g; v = 4.9 m/s; E = 0.74 J

Figure 4.4: Damage states beneath the impact point of the laminate after low-velocity impact [65].

Matrix cracking   Delamination (Interlaminar)

Fiber direction

1 mm

Bending cracks   Overall view   Cone cracks

magnified view i

0.05 mm

magnified view ii

0.05 mm

(c) Specimen 3; m = 62 g; v = 6.0 m/s; E = 1.13 J

Delamination (Interlaminar)   Fiber breakage Crater   Matrix cracking

Delamination (Intralaminar)

Fiber direction

1 mm

Overall view

magnified view i

D   E

0.05 mm

magnified view ii

D   E

0.1 mm
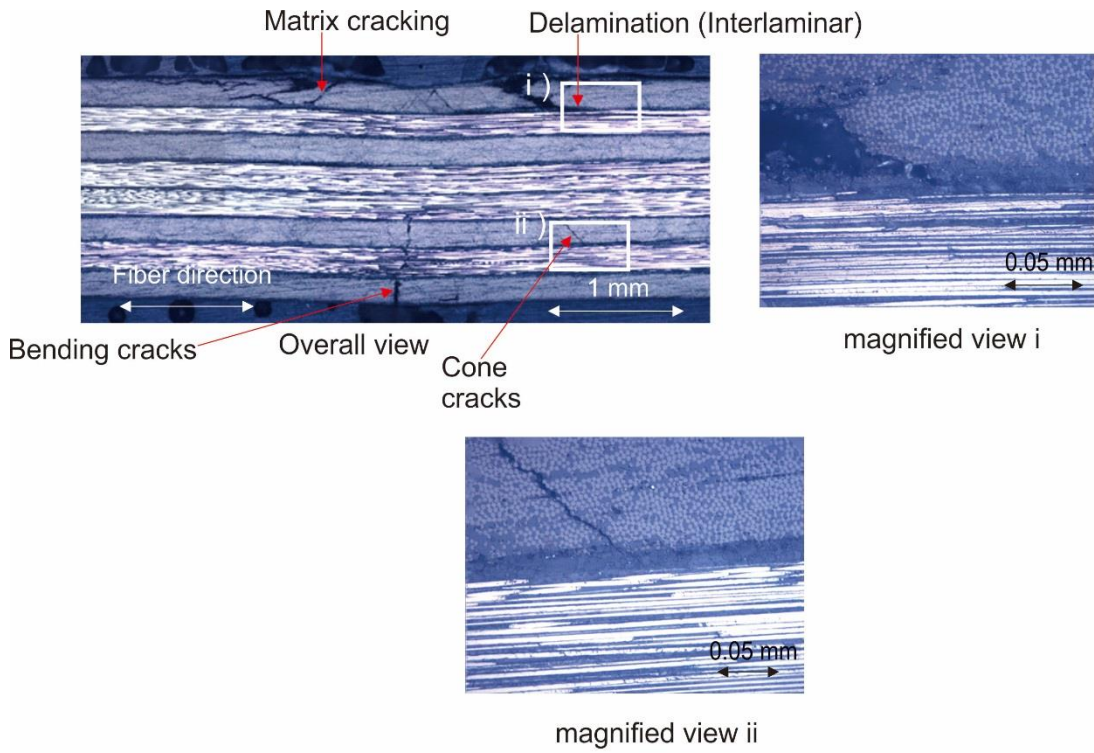
(d) Specimen 4; m = 150 g; v = 6.0 m/s; E = 2.92 J

Figure 4.4: Continued

57
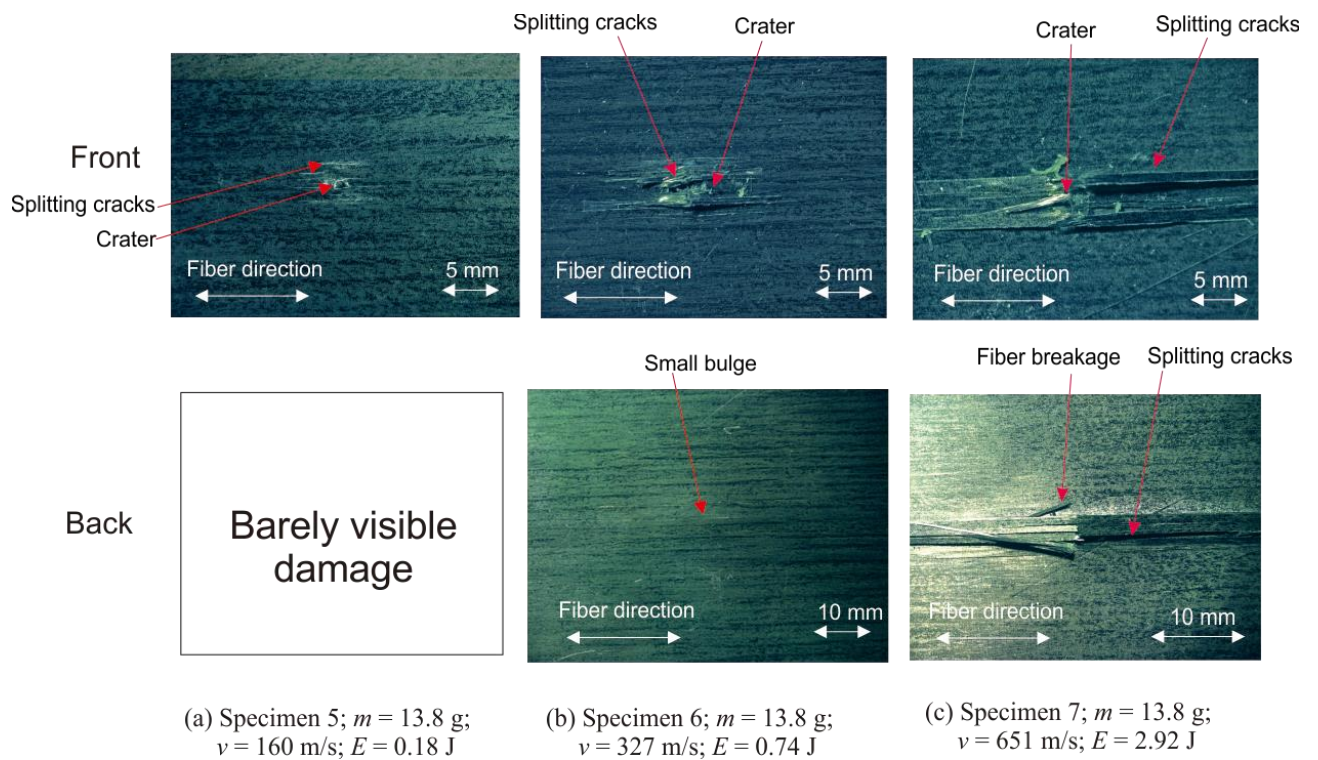
Figure 4.5: Damage on the front and back surfaces of the laminates after high-velocity impact [65].

(a) Specimen 5; m = 13.8 g; v = 160 m/s; E = 0.18 J

(b) Specimen 6; m = 13.8 g; v = 327 m/s; E = 0.74 J

(c) Specimen 7; m = 13.8 g; v = 651 m/s; E = 2.92 J

Figure 4.6 presents soft X-ray photographs of the specimens after the high-velocity impact test. The fiber direction of the top and bottom plies is indicated by the arrow. At lower velocities (Figures 4.6(a) and (b)), the difference of delamination length between the fiber and transverse directions is minor. However, in the specimen after full penetration (Figure 4.6(c)), the delamination is in a galaxy-shape and is much longer in the fiber direction. As a result, the shape of delamination after high-velocity impact is similar to that after low-velocity impact with high impact energy.

58

(a) Specimen 5; v = 160 m/s   (b) Specimen 6; v = 327 m/s   (c) Specimen 7; v = 651 m/s

Figure 4.6: Soft X-ray photographs of the laminates after high-velocity impact [65].

Figure 4.7 shows the cross-sectional views of the damage generated beneath the impact point for three velocities. Even when the impact velocity is relatively low (Figure 4.7(a)), both a crater and matrix cracking are observed in the top ply. In addition, the delamination is also generated at the interface between the interlayer and the base 0° ply (arrow A), not in the interlayer. At a middle impact velocity (Figure 4.7(b)), a crater, matrix cracking including cone cracks and bending cracks and fiber breakage are generated in all the plies. Most delaminations are generated at the interface between the interlayer and the base ply (arrows B) although several cracks are observed inside the interlayer (arrows C).

At the highest impact velocity (Figure 4.7(c)), the specimen exhibits a catastrophic damage state consisting of a crater, matrix cracking and fiber breakage as well as large-scale delamination. It is interesting to note that the intralaminar delamination is generated in the laminate at this velocity only. For example, the delamination at the interface

between the interlayer and the base ply (arrow D) is connected with the intralaminar delamination (arrow E).

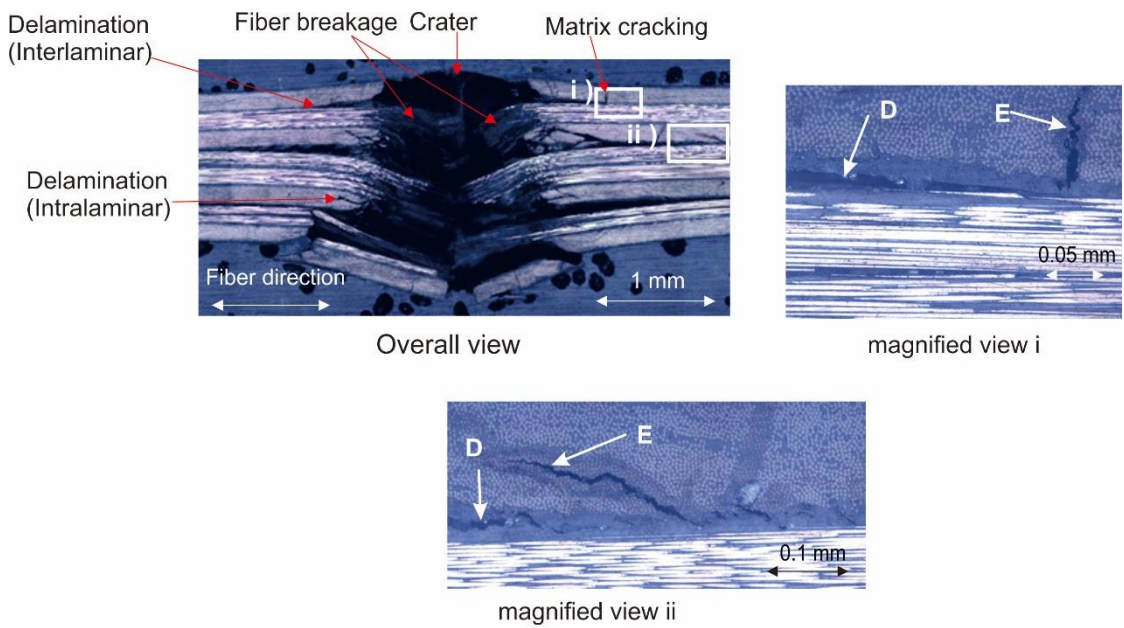(a) Specimen 5; m = 13.8 g; v = 160 m/s; E = 0.18 J

(b) Specimen 6; m = 13.8g; v = 327 m/s; E = 0.74 J

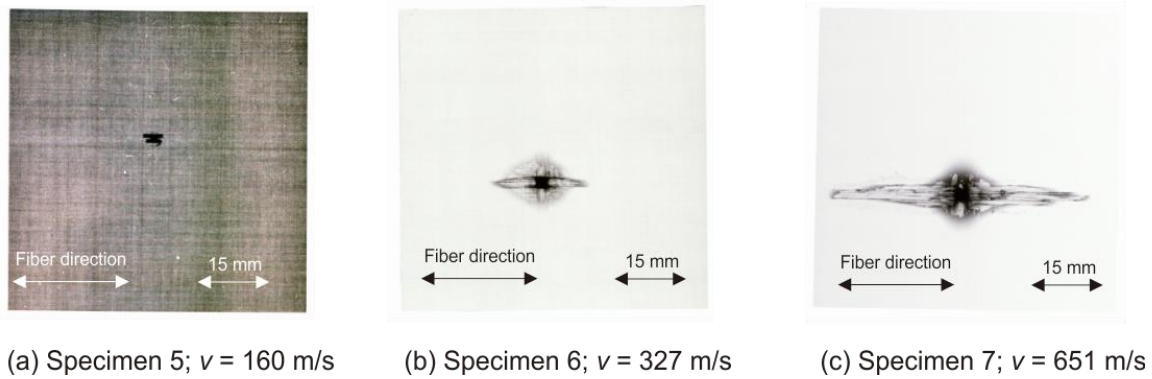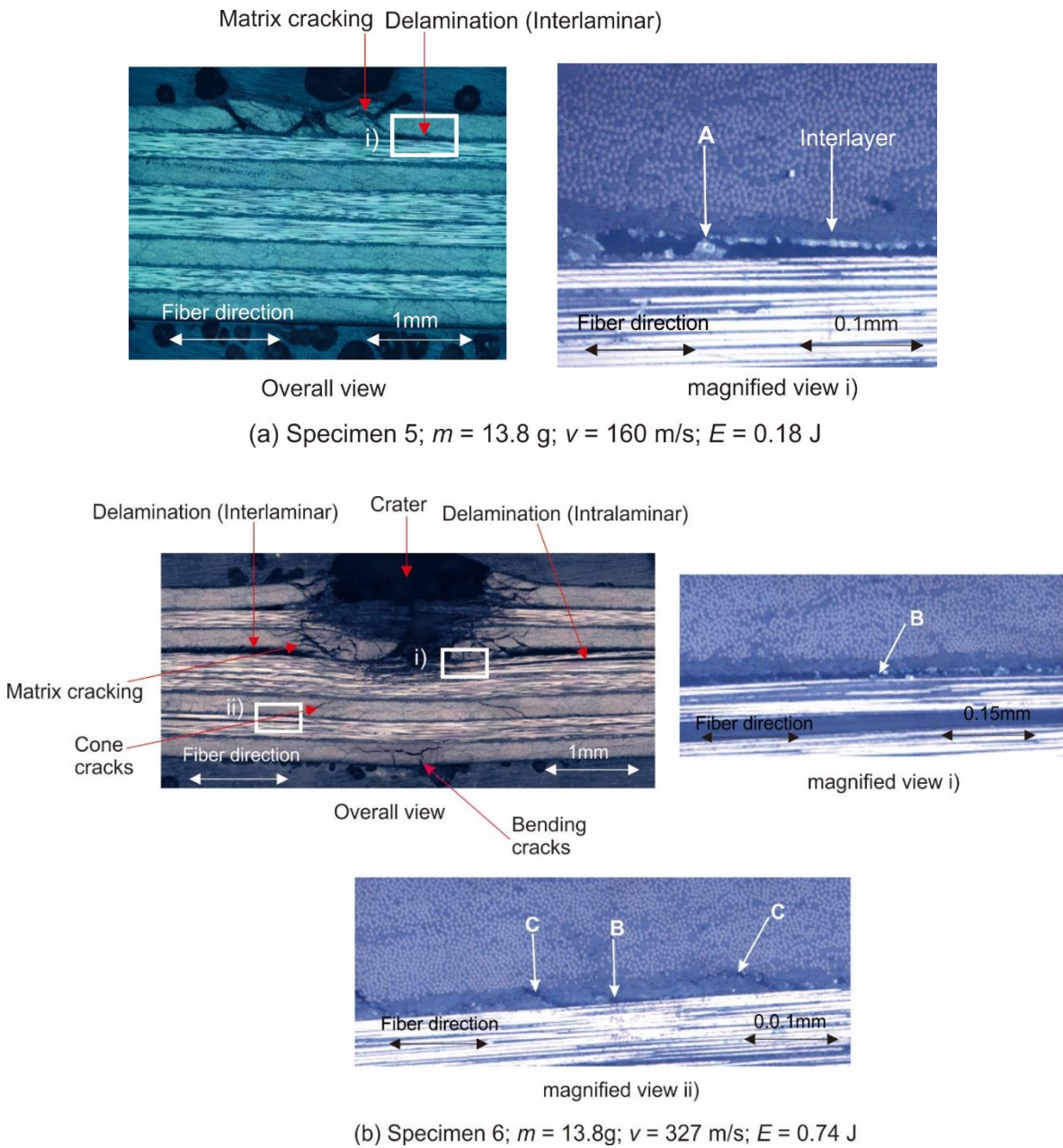Figure 4.7: Damage states beneath the impact point of the laminates after high-velocity impact [65].

60
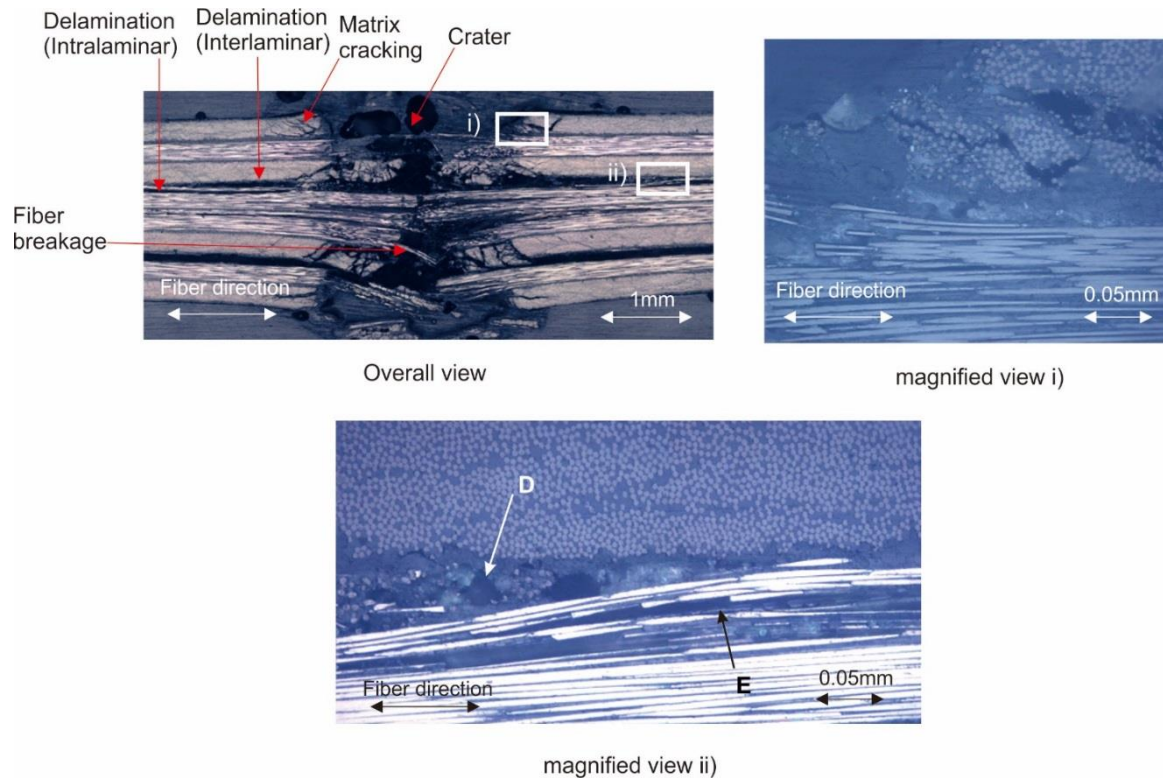
Figure 4.7: Continued

4.4   Comparison of Damage between Low- and High-Velocity Impacts

As shown in the experimental result, low- and high-velocity impacts produce different damage states. The schematic illustrations for low- and high-velocity impacts damage are depicted in Figures 4.8 and 4.9, respectively. The damage mode for low-velocity impact is almost the same as that for high-velocity impact since the damage consists of a dent or crater, matrix cracking, interlaminar delamination, intralaminar delamination and fiber breakage. The delamination shape is also similar between the both impacts although the delamination size is different as shown later.

However, several differences between the two impact damage states are found from the microscopic observations. First, a crater with multiple splitting cracks are generated on the surface of the laminate subjected to high-velocity impact. Similar damage is observed in a general-purpose CFRP laminate [53]. The splitting cracks are generated probably because local delamination beneath the impact point enables the shear deformation of the top surface. In contrast, since such delamination is hardly generated in low-velocity impact, fiber breakage occurs mainly due to compressive stress. Figure 4.10 shows fiber failure in the top ply which is presumed to be due to global deformation of the laminate and the compression of the fiber during the impact [55][56]. Consequently, two cracks propagating in the transverse direction from the dent or crater are generated as shown in Figure 4.1.

Secondly, the splitting cracks on the back surface is observed for both impacts when the impact velocity or energy is high (Figures 4.2 and 4.5). In the low-velocity impact, the global deformation of the laminate produces bending cracks in the bottom ply, which appears as the splitting cracks with bulging on the back surface. On the other hand, in the high-velocity impact, local bending-induced tensile stress causes multiple splitting cracks together with fiber breakage on the back surface [33].
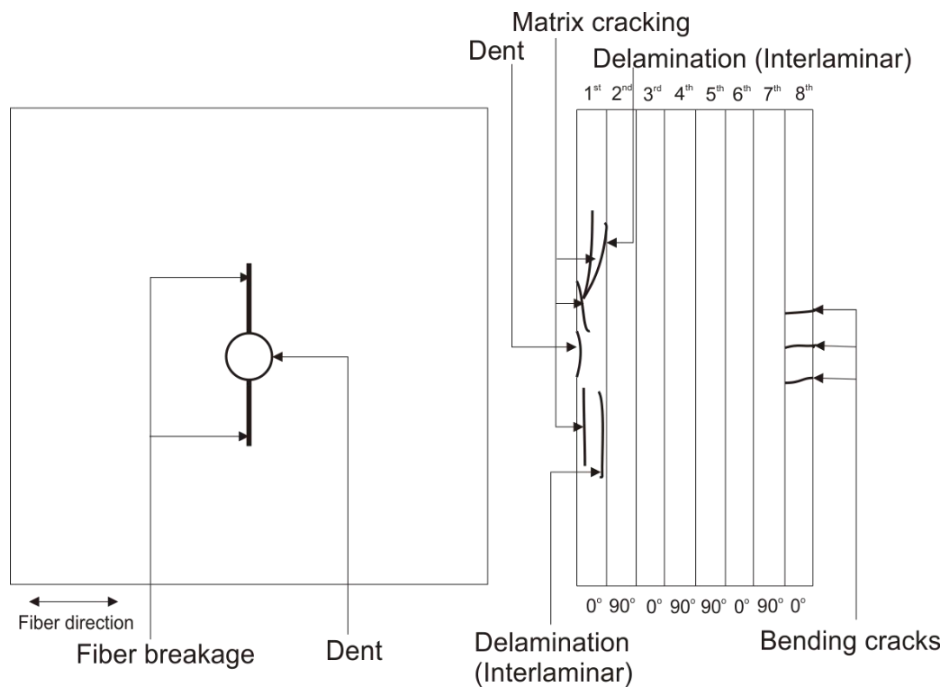
(a) Specimen 2: $m = 62$ g; $v = 4.9$ m/s; $E = 0.74$ J
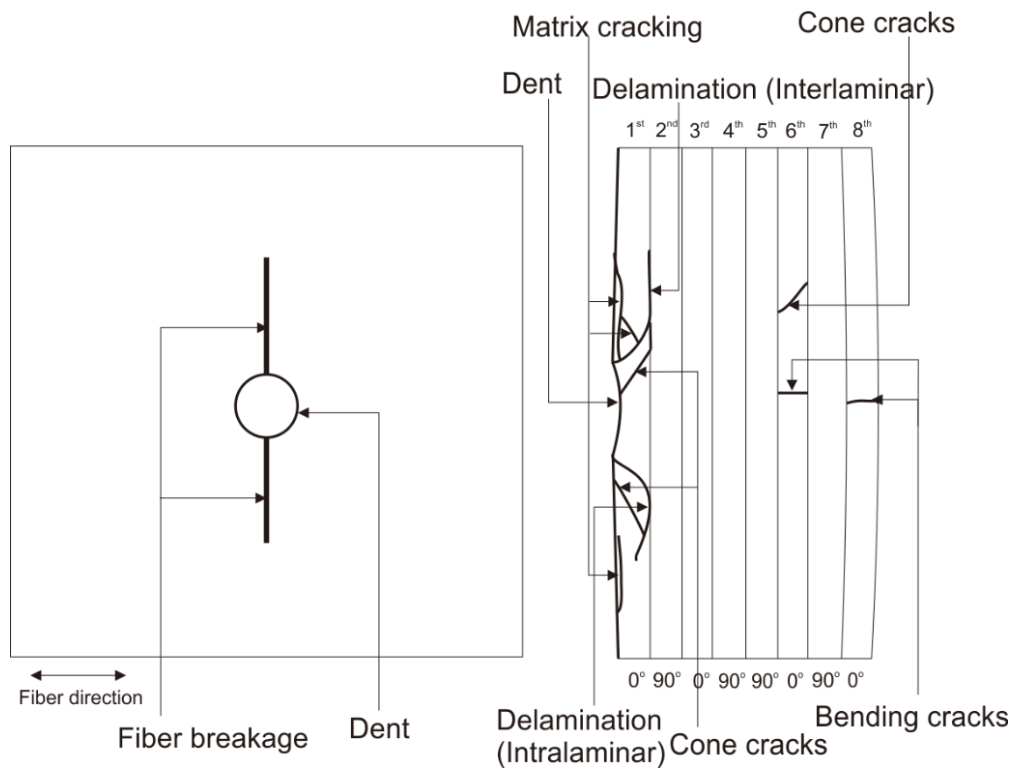
(b) Specimen 3: $m = 62$ g; $v = 6.0$ m/s; $E = 1.13$ J

Figure 4.8: Schematic diagrams of low-velocity impact damage [65].
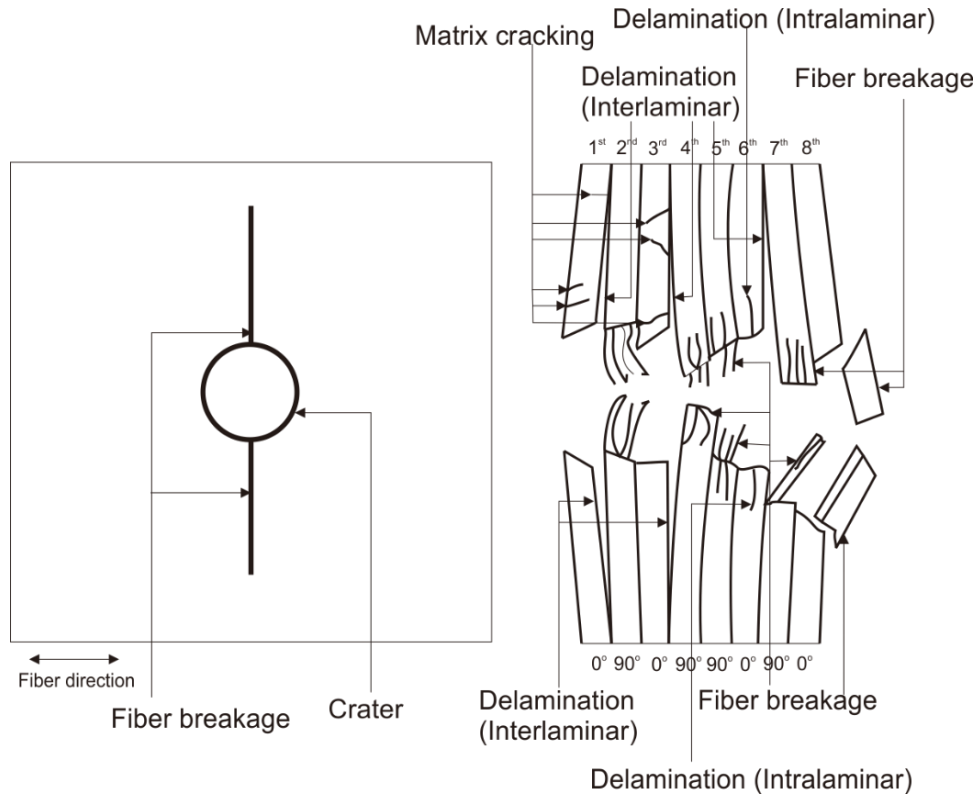
(c) Specimen 4: $m = 150$ g; $v = 6.0$ m/s; $E = 2.92$ J

Figure 4.8: Continued.

(a) Specimen 5: $m = 13.8$ g; $v = 160$ m/s; $E = 0.18$ J
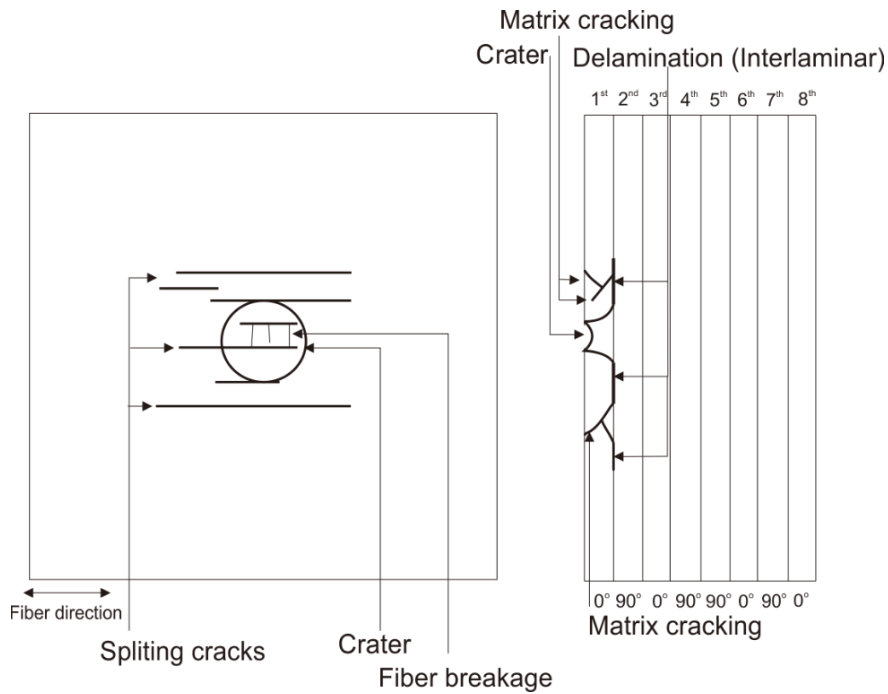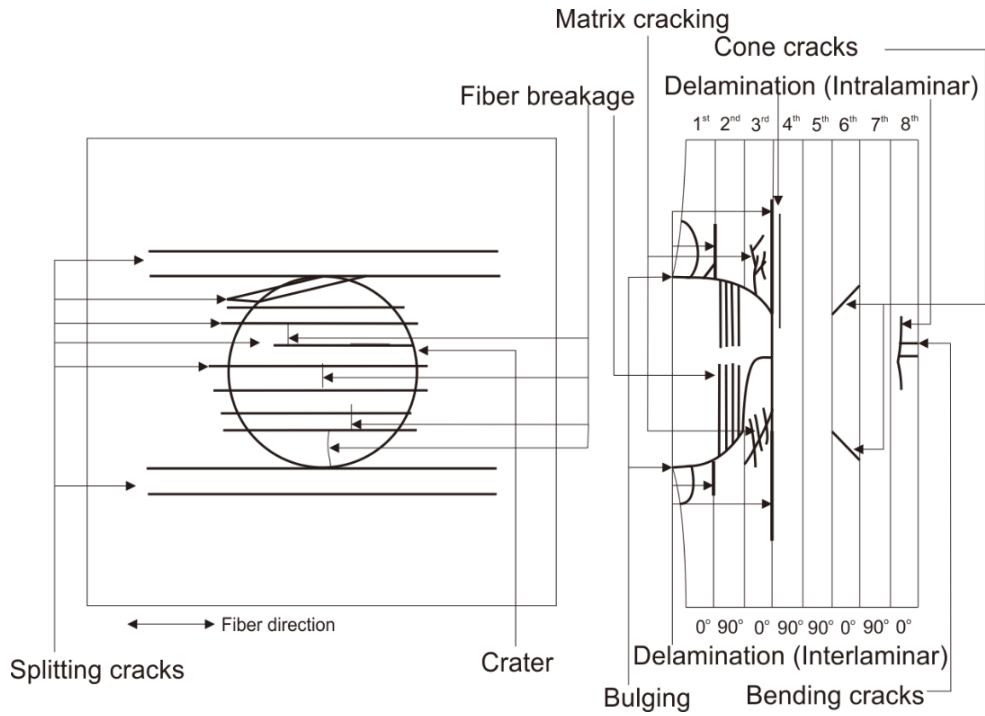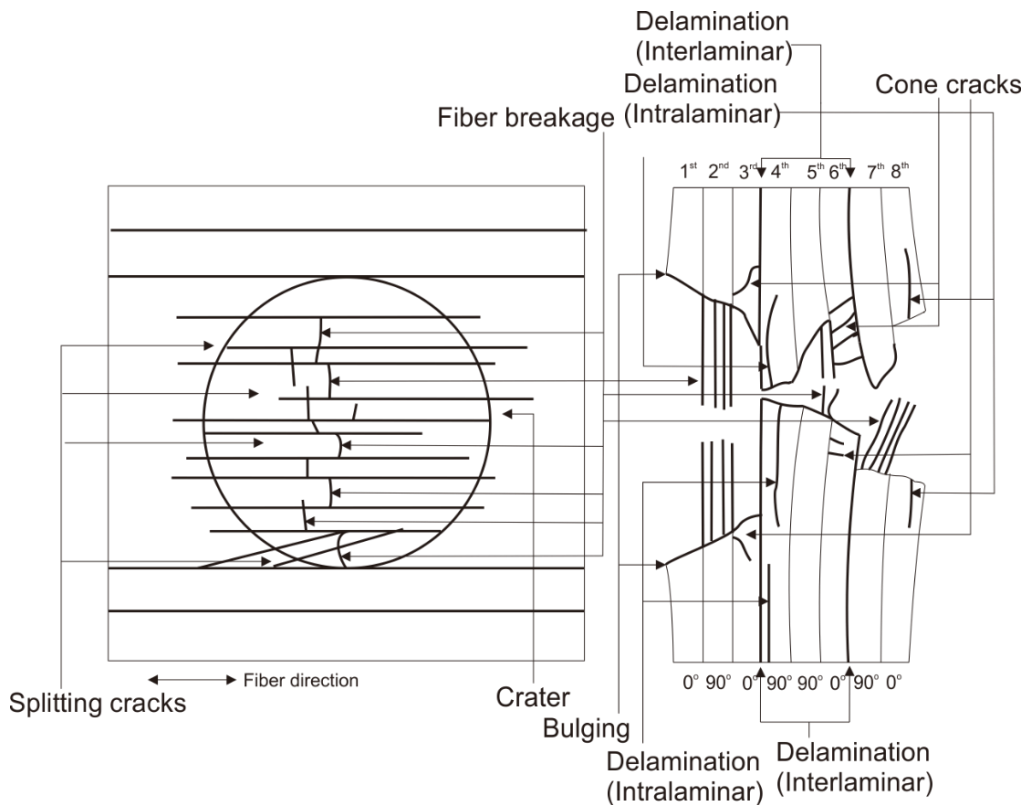
Figure 4.9: Schematic diagrams of high-velocity impact damage [65].

(b) Specimen 6: $m = 13.8$ g; $v = 327$ m/s; $E = 0.74$ J

(c) Specimen 7: $m = 13.8$ g; $v = 651$ m/s; $E = 2.92$ J

Figure 4.9: Continued.

Thirdly, the damage state for the same impact energy but different impact velocity is discussed. From Figures 4.4(b) and 4.7(b) ($E = 0.74$ J), the damage state in the high-velocity impact seems to be much more severe than that in the low-speed impact. In the high-velocity impact, a deep crater, delamination, cone cracks and bending cracks are observed from the top to the bottom plies in that order. In contrast, in a low-velocity case, a dent, matrix cracking and delamination are generated only in the top ply in addition to a few bending and cone cracks in the lower plies.

In general, the energy balance during impact is expressed as;

$$E_{impact} = E_{rebound} + E_{damage} + E_{dissipated} \qquad (4.1)$$

where E_{impact} denotes the incident impact energy, $E_{rebound}$ the kinetic energy of the rebounding impactor, E_{damage} the energy consumed by generation of damage and $E_{dissipated}$ the energy dissipated as vibration, heat, inelastic deformation of the impactor or the fixture and so on [57]. In the low-velocity impact without full penetration, $E_{dissipated}$ is relatively larger than E_{damage} due to global deformation while E_{damage} is dominant in the high-velocity impact because of local deformation [54]. As a result, the degree of damage becomes greater in the high-velocity than in the low-velocity impact for the same incident impact energy. However, when full penetration (Figures 7(d) and 10(c) ($E = 2.92$ J)) occurs, the damage state is very similar. This is probably because the

ratio of E_{damage} to E_{impact} increases with increasing impact velocity in the low-velocity impact test.

Finally, delamination area for both impacts is plotted against incident impact energy in Figure 4.11. The delamination area increases with impact energy for both impacts. Contribution of matrix cracking to energy dissipation is supposed to be small. Fiber breakage requires greater impact energy, however, fiber breakage area is much smaller than delamination area. Accordingly, the energy dissipation due to damage is mainly done by delamination. Moreover, as mentioned above, most part of the incident impact energy is consumed by damage generation in the high-velocity impact since the deformation is local. In contrast, the greater part of incident impact energy is absorbed by global deformation in the low-velocity impact. As a result, the high-velocity impact exhibits delamination area larger than the low-velocity impact for the same incident impact energy. In addition, Figure 4.11 indicates that the threshold incident impact energy is approximately 0.18 J for both impacts. Numerical simulation including interlayers is necessary to quantitatively discuss the damage behavior and will be made in future work.
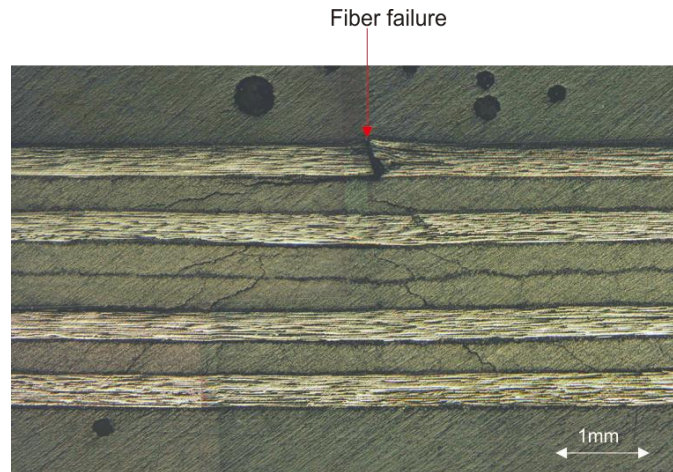
Figure 4.10: Fiber failure after low-velocity impact [65].

4.5   The Influence of Toughened Interlayers

The interlayers have a significant effect on both low- and high-velocity cases. It is found from the microscopic observation that matrix cracking due to low-velocity impact is clearly arrested by the interlayers (see the magnified views in Figures 4.4(b) and (c)). However, in the low-velocity impact with high energy and the high-velocity impact, matrix cracking does not always stop at the interlayer. This result suggests that matrix cracking propagates to the interlayers when the impact energy density (impact energy per volume) is greater than a critical value. In this case, impact energy cannot be fully dissipated by cracking and plastic deformation of the interlayers.

As shown in Figure 4.7(c), interlaminar delamination sometimes transits to intralaminar delamination. The Mode I interlaminar fracture toughness of a similar composite laminate (T800H/#3900-2) is about three times as conventional CFRP

laminates (T800H/#3631) [58]. This high interlaminar fracture toughness causes the transition of the delamination in the toughened interlayer to that in the untoughened base ply.

Figure 4.12 depicts the surface of delamination between the 7th and 8th plies just below the impact point in the specimen after the low-velocity impact with the highest impact energy ($E = 2.92$ J). The resin rich region is prominent on this fracture surface although the base ply (arrow A) is partly observed. From this figure, it is concluded that the delamination propagates at the interface between the bottom (7th) interlayer and the bottom (8th) base ply. The fracture mode seems to be brittle because the surface exhibits little plastic deformation. The delamination initiation and propagation modes below the impact point are rather complicated because not only the stress state but also the damage process can affect the modes. At the present stage, it can be said from the previous numerical simulation [33] that Mode II propagation becomes dominant as the delamination propagates away from the impact point.
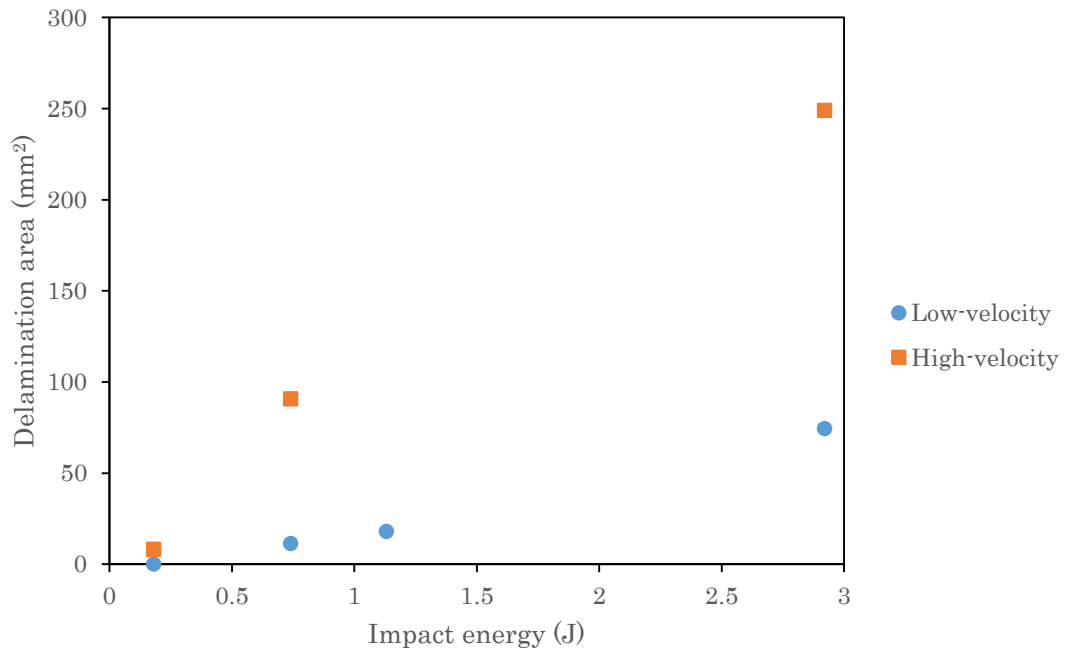
Figure 4.11: Relationship between delamination area and impact energy for low- and high-velocity impacts [65].
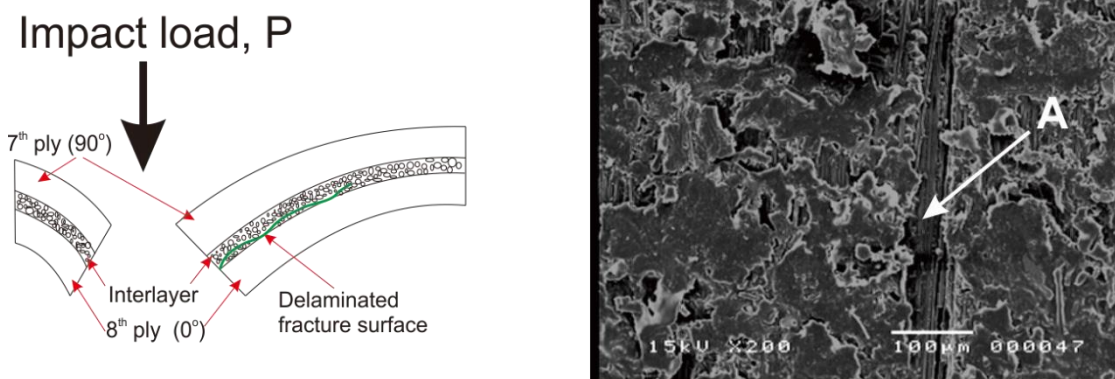
Figure 4.12: SEM photo showing the surface of delamination in the specimen after the low-velocity impact [65].

4.6   Summary of the Chapter

The low-velocity and high-velocity impact damage in CFRP with toughened interlayers was experimentally characterized in this chapter. Based on the results obtained, it can be summarized as follows:

1. The splitting cracks on the front surface of the laminate propagate in the fiber direction in the high-velocity impact. In contrast, in the low-velocity impact, the cracks normal to the fiber direction are generated on the front surface.

2. The interlaminar delamination tends to propagate in the fiber direction for both impacts, resulting in a galaxy shape delamination.

3. The degree of damage is relatively large in the high-velocity impact even though the deformation is localized. In contrast, in the low-velocity impact, the damage is relatively mild because the ratio of dissipated energy to incident impact energy is larger than in the high-velocity impact.

4. The interlayers suppress the delamination when the incident impact energy is smaller than the threshold value (approximately 0.18 J). The high fracture toughness of the interlayers sometimes produces the transition of interlaminar delamination to intralaminar delamination.

CHAPTER 5: EXPERIMENTAL AND NUMERICAL CHARACTERIZATION OF LOW-VELOCITY IMPACT DAMAGE OF A CFRP LAMINATE WITH TOUGHENED INTERLAYERS

5.1   Introduction

Composite materials such as carbon fiber reinforced plastics (CFRPs) have been used in various engineering applications in aircraft structure due to high specific strength and modulus. Nonetheless, CFRP is still vulnerable to damage induced by out-of-plane impact loading since such damage may reduce the strength and the stiffness of CFRP. The damage due to low-velocity impact can be in the form of clearly visible impact damage (CVID) or barely visible impact damage (BVID). The latter would be of concern since the small indentations may be created on the laminate surface, covering the internal damage which can have significant effect on strength, durability and stability[17][20][39][59][60][61]. Therefore, the characterization of damage is essential to improve the reliability of CFRP when subjected to low-velocity impact.

The low-velocity impact damage behavior of composite materials has been studied by many researchers. Abrate [39] made a comprehensive review on various low-velocity impact tests and their related damage mechanisms. In an extensive review by Richardson

and Wisheart [59], the damage processes and modes of failure may differ depending on the type of material systems. Hossaienzadeh et al. [14] compared the impact damage among several fiber reinforced materials and proved that the damage area grows unpredictably in CFRP with the increase of impact energy.

In order to improve the damage resistance and interlaminar fracture toughness of laminated composites, an interlayer is often introduced by replacing resin at prepreg surface to a tougher system such as the inclusion of thermoplastic particles [6]. Lee et al. [7] reported that modes I and II interlaminar fracture toughness increased after adding the tough adhesive layers. In spite of these studies, the microscopic damage extension of such CFRP laminate due to impact is still unclear and requires further investigation.

Several numerical studies [24][62][28][63] have been performed to model the damage and failure mechanism generated in composite laminates. For example, the following models have been proposed: the continuum damage mechanics (CDM) model that is based on damage initiation and evolution, the fracture mechanics approach and the equivalent constraint model (ECM). Furthermore, there is also a study on multi-scale modelling, where the macro-, meso- and micro-scale behavior of the impact failure was integrated based on the generalized method of cells (GMC) [28]. The cohesive zone model (CZM) was also used to predict low-velocity impact damage [64]. The cohesive

elements were inserted between the solid elements to represent cracks and delamination. Therefore, the CZM model could also be applied to the impact damage process of CFRPs with interlayers if they have similar damage behavior. Recently, Othman et al. [65] has studied a comparison between low-velocity and high-velocity impact damage on a CFRP laminate with interlayers and found that its damage mode is similar to that of laminates without interlayers. However, numerical simulation needs to be carried out for further quantitative investigation through comparison with experimental result.

This chapter aims at characterizing the microscopic damage behavior of a CFRP laminate with toughened interlayers subjected to low-velocity impact. First, a low-velocity impact test was conducted to reveal the damage state for various impact velocities and energies as summarized in Table 5.1. Next, numerical analysis was performed to clarify the impact damage mechanisms through comparison with experiment results for one typical impact velocity (specimen 1).

5.2   Microscopic Damage State

Figure 5.1 depicts the damage state generated beneath the impact point of the specimen. It should be noted that the fiber (0°-) direction in the top and bottom plies of the laminate are normal to the photographs. The damage consists of a dent, delaminations

and matrix cracks including bending cracks in the bottom ply and cone cracks in the

middle ply. In the top ply, both interlaminar and intralaminar delaminations are generated.

The interlaminar delamination extends between the top ply and the interlayer, whereas

the intralaminar one is inside the top ply (arrow A in Figure 5.1(b)).

Table 5.1: Experimental specimens

Specimen	Mass of impactor, m (g)	Height, H (m)	Velocity, v (m/s)	Incident impact energy, E (J)
Specimen 1	70.4	1.30	5.05	0.90
Specimen 2	70.4	2.00	6.26	1.38
Specimen 3	150.3	1.80	5.94	2.65
Specimen 4	70.4	0.49	3.1	0.34
Specimen 5	70.4	0.70	3.71	0.48
Specimen 6	150.3	1.00	4.43	1.47
Specimen 7	150.3	1.40	5.24	2.06
Specimen 8	150.3	1.98	6.23	2.92

As shown in Figure 5.1(d), the intralaminar delamination is generated between the

resin-rich and fiber-rich regions in the top ply. Most of the matrix cracks stop at the

interface between the base ply and the interlayer (arrow B in Figure 5.1(c)). The cracks

propagate among the thermoplastic particles to make a tortuous path (Figure 5.1(e)).

Consequently, the interlayer acts as a crack arrestor and a deflector.

In contrast, the conventional CFRP without the interlayers exhibits interlaminar delamination only [20][65]. The intralaminar delamination in the laminate with interlayers is attributed to interlaminar fracture toughness higher than intralaminar one.
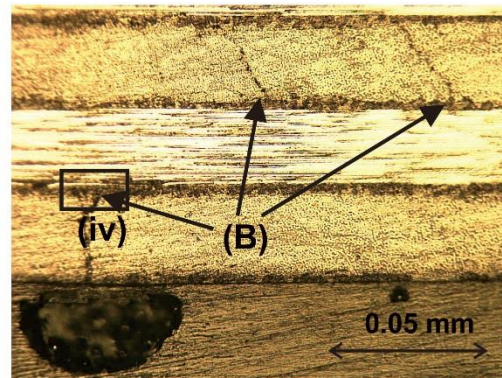

(a) Overall view Specimen 1; m = 70.4 g; v = 5.05 m/s; E = 0.9 J

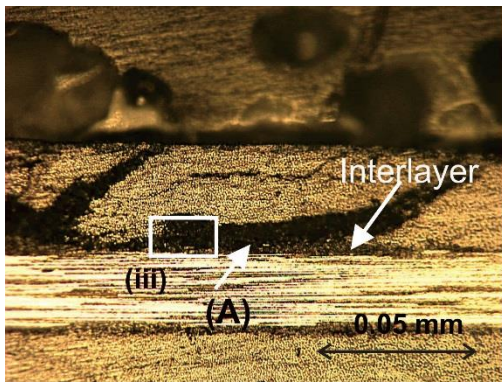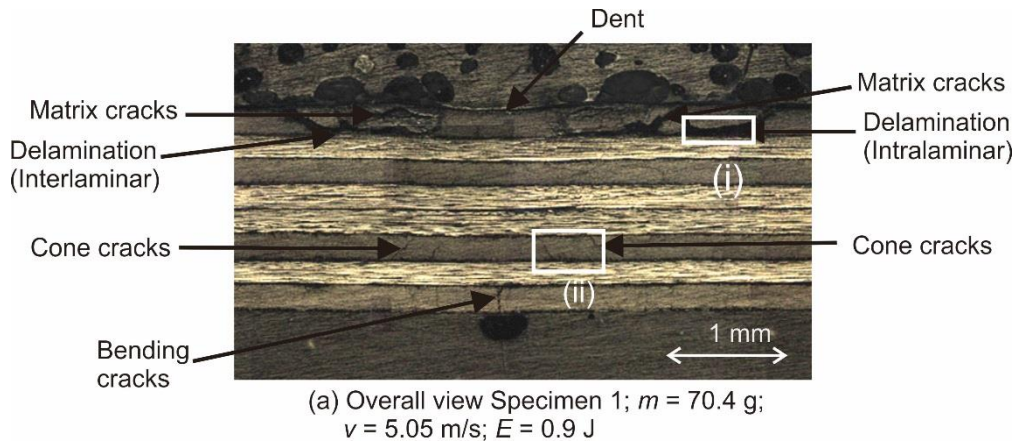(b) magnified view (i)

(c) magnified view (ii)

Figure 5.1: Damage states beneath the impact point of the specimen 1 laminate after low-velocity impact [66].
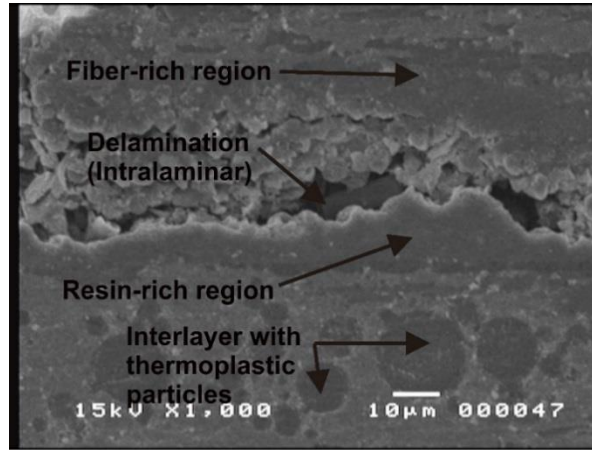
(d) SEM photo for the magnified view (iii)
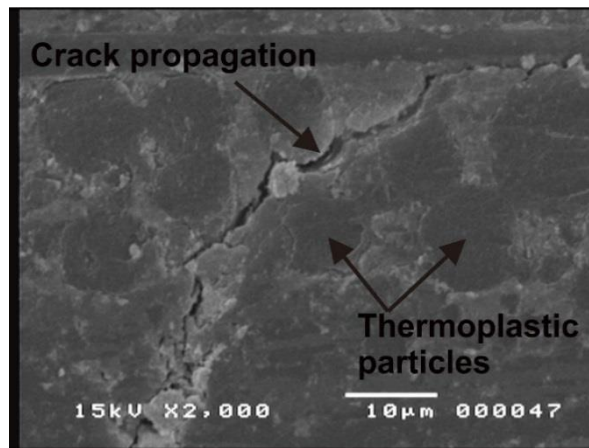
(e) SEM photo for the magnified view (iv)

Figure 5.1: Continued.

Additionally, the matrix damage in the laminate is intensively simulated by observing

cross sectional view as depicted in Figure 5.2. Based on the figure, much of matrix cracks

are due to tensile stress in transverse direction as well as shear stress. At the bottom ply,

bending cracks are also generated because of tensile stress and shear stress during bending

deformation. Nevertheless, the cone cracks are not reproduce in this modelling since it is

considerably difficult to model cone cracks in solid element only.

SDV10
(Avg: 75%)

+1.400e+01
+1.283e+01
+1.167e+01
+1.050e+01
+9.333e+00
+8.167e+00
+7.000e+00
+5.833e+00
+4.667e+00
+3.500e+00
+2.333e+00
+1.167e+00
+0.000e+00

Transverse tensile stress

Transverse compressive stress

Default

In-plane shear stress

Out-of plane shear s

2mm

Figure 5.2: The cross sectional view of simulated matrix damage of specimen 1 after low-velocity impact.

Figure 5.3 depicts the damage behavior at impact velocity of $v = 6.26$ m/s and impact energy, $E = 1.38$ J. The damage state is similar with in Fig. 5(a) although the number and propagation of matrix cracks and cone cracks are relatively higher. In addition, both interlaminar and intralaminar delamination are also generated. Interlaminar delamination is observed at the interface between 0° ply and the interlayer as depicted in the magnified view i (arrow C). In contrast, intralaminar delamination is denoted by the lateral crack generated on the 0° ply as shown in the magnified view ii (arrow D).
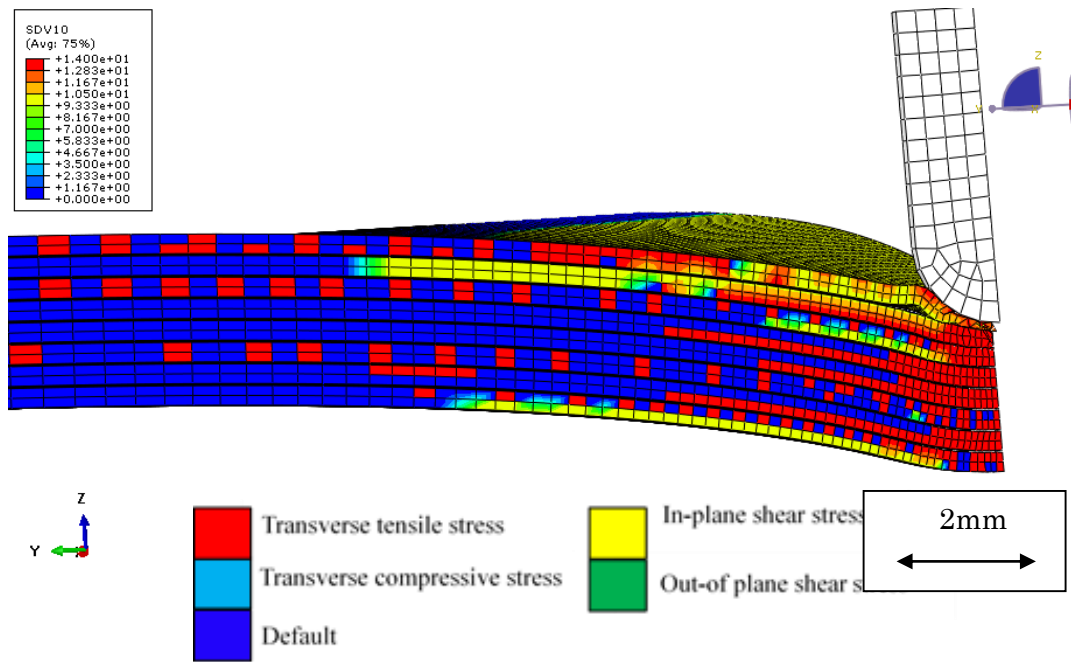
Figure 5.3: Damage states beneath the impact point of the specimen 2 laminate after low-velocity impact.

Another impact damage state is depicted in Figure 5.4 with $v = 5.94$ m/s and $E = 2.65$ J. At this state, full penetration is generated because the impact energy is higher due to increasing mass of impactor. The top surface area of laminate beneath the impact point exhibits a crater with bulging and all plies including the interlayers break in the perforation region. In the vicinity area of penetration; fiber breakage, interlaminar and intralaminar delamination as well as matrix cracks are generated. As depicted in the magnified view (i) (Figure 5.4(b)), it is observed that the interlaminar delamination is

generated at the interface between the interlayer (bottom interface) and base ply (90°) (arrow E) and it is differ from specimen 2 damage (Figure 5.3(b)) since the interlaminar delamination is generated at the interface between 0° ply and interlayer (top interface).

The interlaminar delamination is generated due to plastic deformation of interlayer as depicted in Figure 5.4(d). Apart from interlaminar delamination, intralaminar delamination is also slightly different from specimen 2 because the delamination is generated at base ply (90°) as depicted in the magnified view (ii) (arrow F) (Figure 5.4(c)). Consequently, the presence of the toughened interlayer generated an intralaminar delamination as it is not observed in conventional CFRP. Furthermore, the transition from interlaminar delamination to intralaminar delamination indicates high interlaminar fracture toughness in the toughened interlayer to that in the untoughened base ply [65].

5.3   Front and Back Surface Damage

Figure 5.5(a) depicts the damage states on the front surface of the laminate. The laminate has a dent with two fiber-breaking cracks propagating in the transverse (90°-) direction, while any splitting cracks parallel to 0°-direction are not generated. A similar damage pattern is simulated as depicted in Figure 5.5(b) where the dent (arrow A) and cracks (arrow B) are generated on the front surface. These cracks (fiber breakage) are

ascribed to compressive stress in the 0°-direction, which causes buckling of carbon fiber.
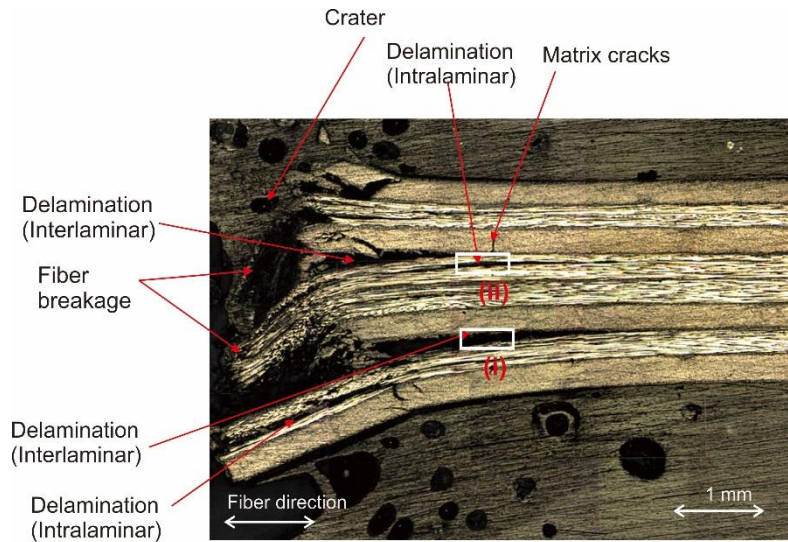
(a) Overall view Specimen 3; m = 150.3 g;
v = 5.94 m/s; E = 2.65 J
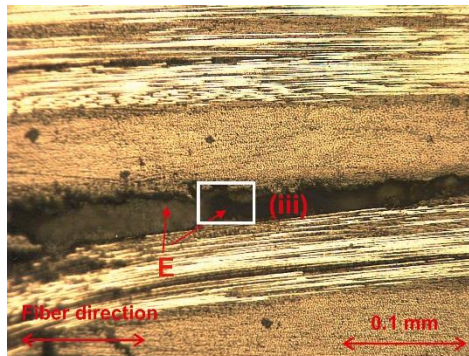
(b) magnified view (i)
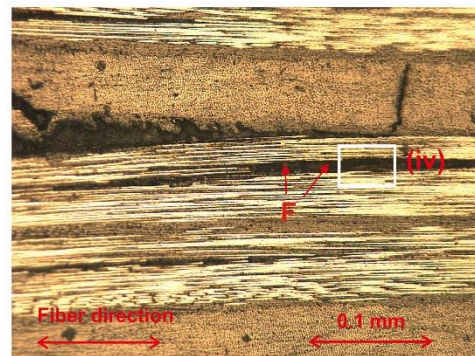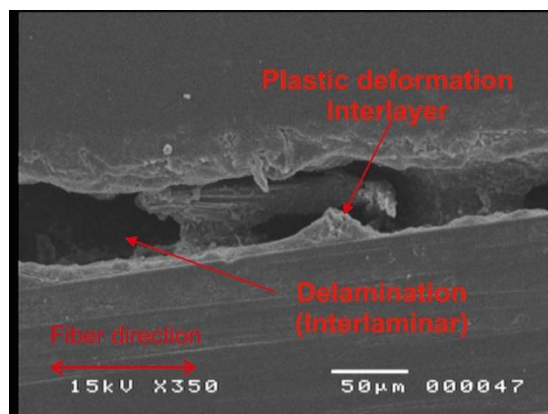
(c) magnified view (ii)

(d) SEM photo for magnified view (iii)

Figure 5.4: Damage states beneath the impact point of the specimen 3 laminate
after low-velocity impact.
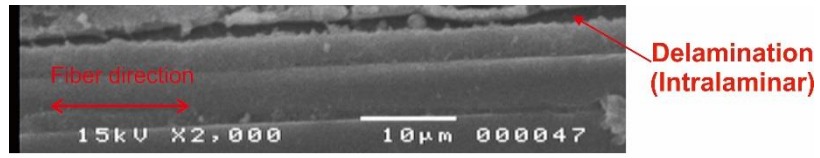
(e) SEM photo for magnified view (iv)

Figure 5.4: Continued.
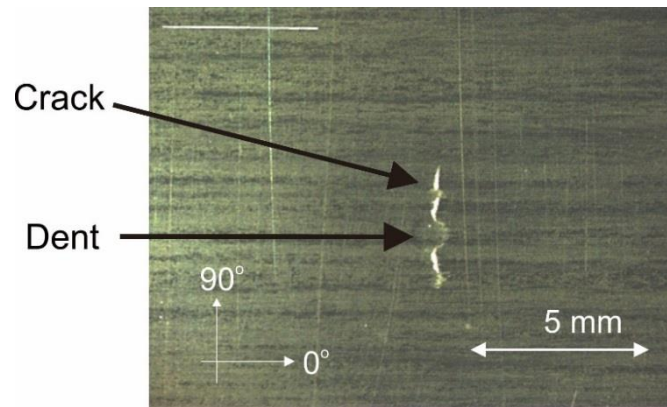
(a)
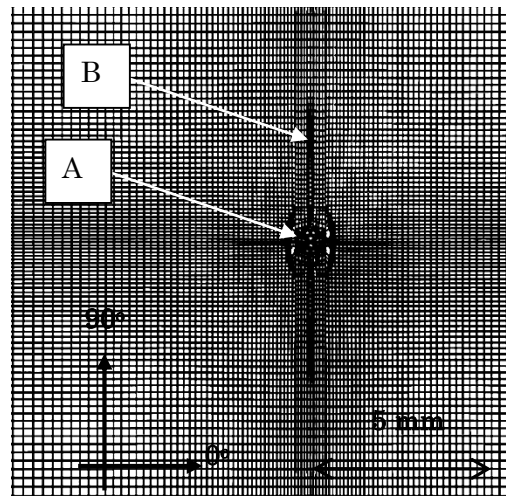
(b)

Figure 5.5: Damage on the front surface of the specimen 1 laminate after impact;
(a) Experimental result, (b) simulation result [66].

On the contrary, the bulging area is generated on the back surface of the laminate and the crack propagates in the 0°-direction (Figure 5.6(a) and arrow C in Figure 5.6(b)). The bulging is due to bi-axial tensile stress in the 0°- and 90°-directions due to global bending deformation of the specimen.

Similar damage pattern was observed at the front and back surfaces of the laminate for other impact energies as depicted in Figure 5.7.
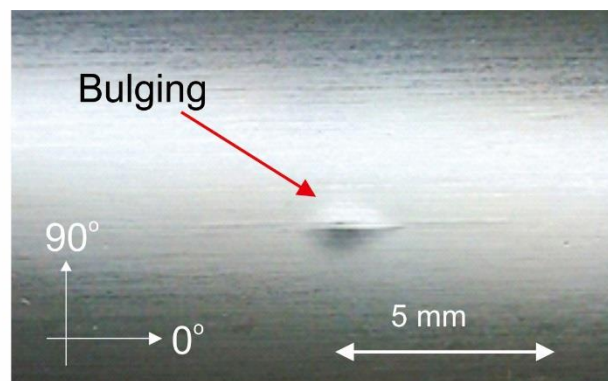
(a)
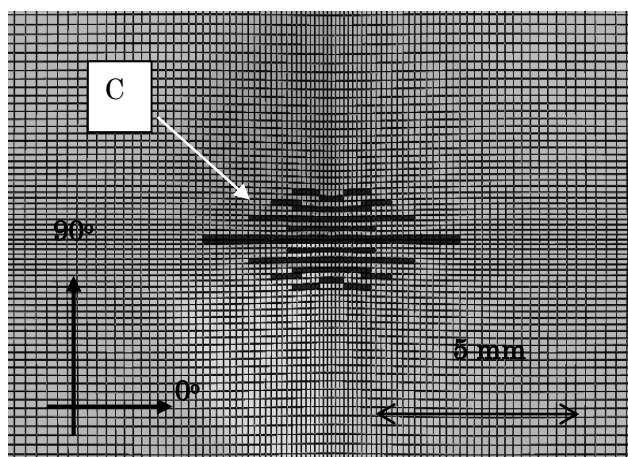
(b)

Figure 5.6: Damage on the back surface of the specimen 1 laminate after impact;
(a) Experimental result, (b) simulation result [66].

Front surface

Crack
Dent

Fiber direction   5 mm

(a)

Crack
Crater

Fiber direction   5 mm

(b)

Back surface

Bulging

Fiber direction   5 mm

(c)

Bulging

Fiber direction   5 mm

(d)
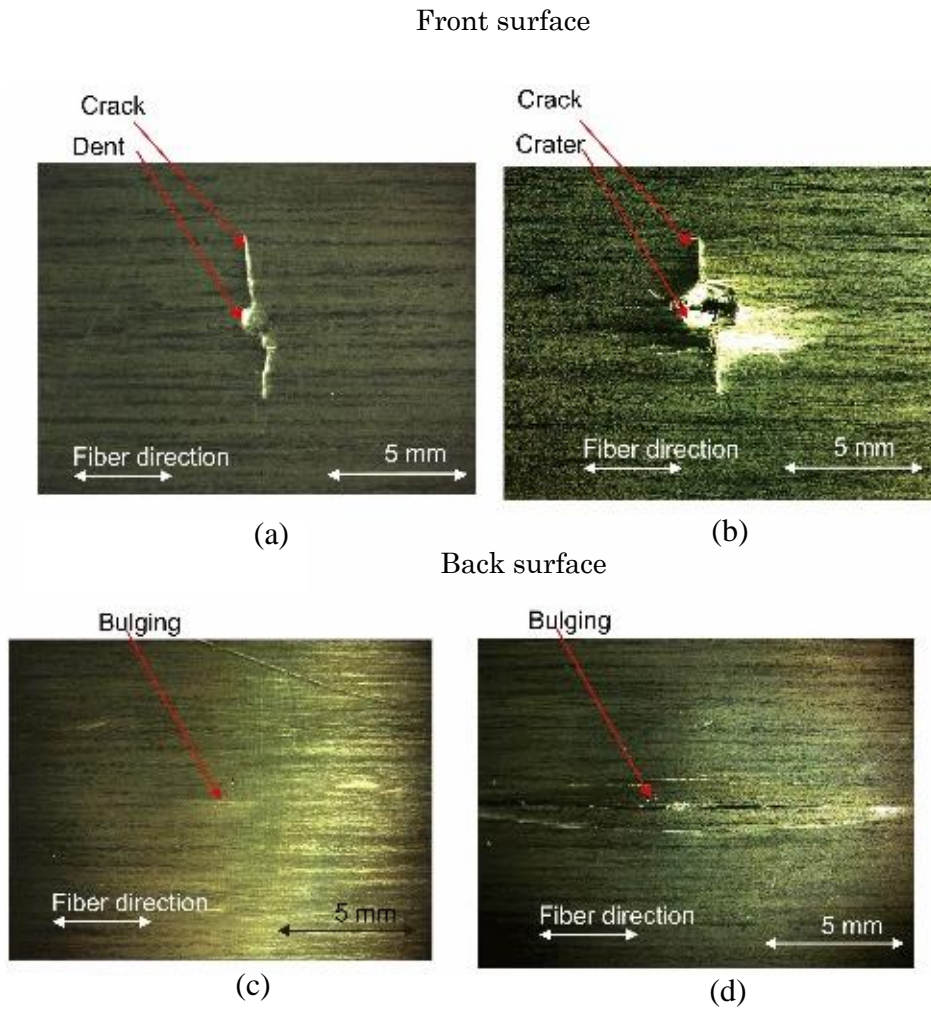
Figure 5.7: Damage on the front and back surface of the laminate after impact; (a)
& (c): specimen 2; (b) & (d): specimen 3.

5.4   Delamination

A typical soft-X ray photograph of the specimen 1 laminate is presented in Figure
5.8(a). The delamination propagates in both the 0°- and 90°-directions. This delamination
pattern is fairly well reproduced by the simulation in Figure 5.8(b). Figure 5.9
demonstrates the simulated cross sectional view of the specimen after impact. Both the
interlaminar (arrows D) and intralaminar delaminations (arrows E) are generated and

extend in both the 0°- and 90°-directions (X and Y directions in Figure 5.5). The delaminations are remarkable in the upper plies rather than in the lower plies. The same tendency is observed in the experiment (Figure 5.1(a)). Table 5.2 compares the projected delamination area between the experiment and simulation. It should be noted that this delamination includes not only the interlaminar but also the intralaminar ones inside the laminate. The delamination area is slightly overestimated partly because matrix failure inside the interlayers are not taken into account in the simulation.
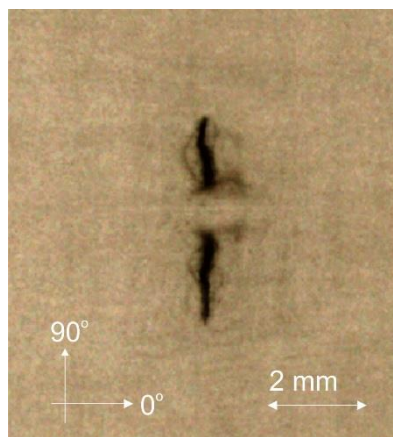
(a)
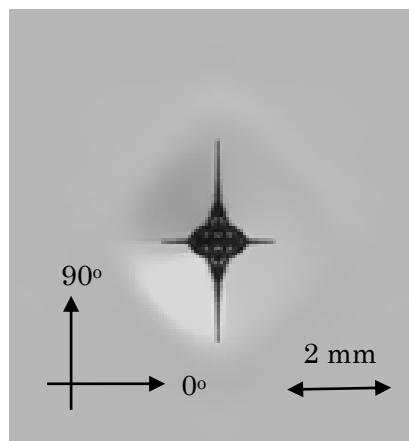
(b)

Figure 5.8: Delamination after impact of specimen 1; (a) Soft X-ray photograph, (b) simulation [66].

On the contrary, the delamination of conventional CFRP without interlayers exhibits

a peanut-shaped delamination[10]. This pattern is different from that in the laminate with

toughened interlayers where the intralaminar delamination is also observed.
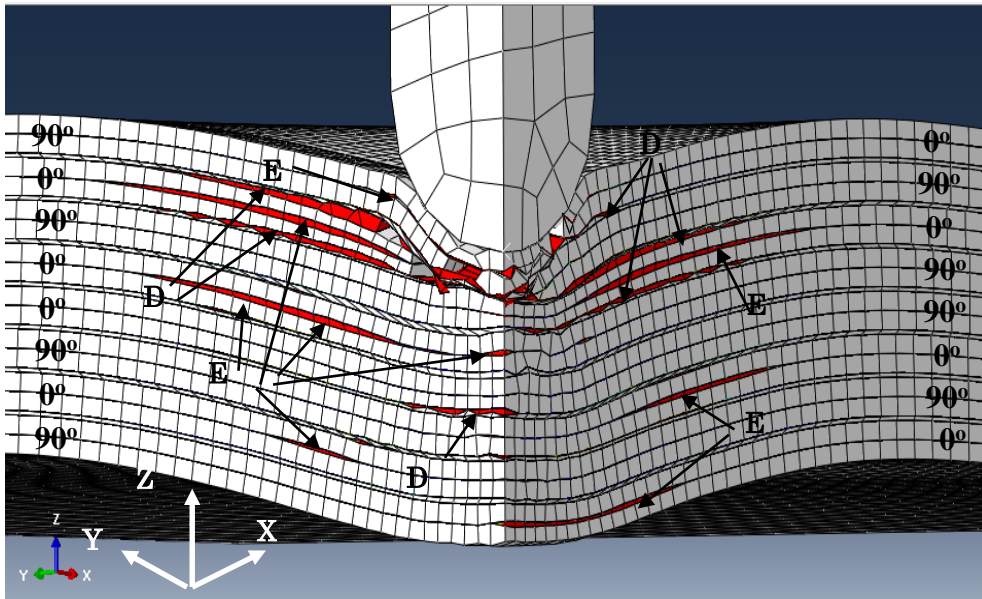
Figure 5.9: Simulated cross sectional view of specimen 1 showing interlaminar
(arrows D) and intralaminar (arrows E) delaminations [66].

Table 5.2: Comparison of projected delamination area of specimen 1 between the
experiment and simulation.

Experiment	Simulation
3.8 mm^2	4.8 mm^2

Figure 5.10 depicts the delamination propagation of specimen 2 and specimen 3

laminate after the impact. Based on the figure, specimen 2 illustrates similar pattern with

specimen 1 but with relatively larger delamination area. On the contrary, the specimen 3

86

laminate displays a galaxy-shape delamination due to full penetration during the impact.

(a) Specimen 2; m = 70.4 g;
v = 6.26 m/s; E = 1.38 J

(b) Specimen 3; m = 150.3 g;
v = 5.94 m/s; E = 2.65 J
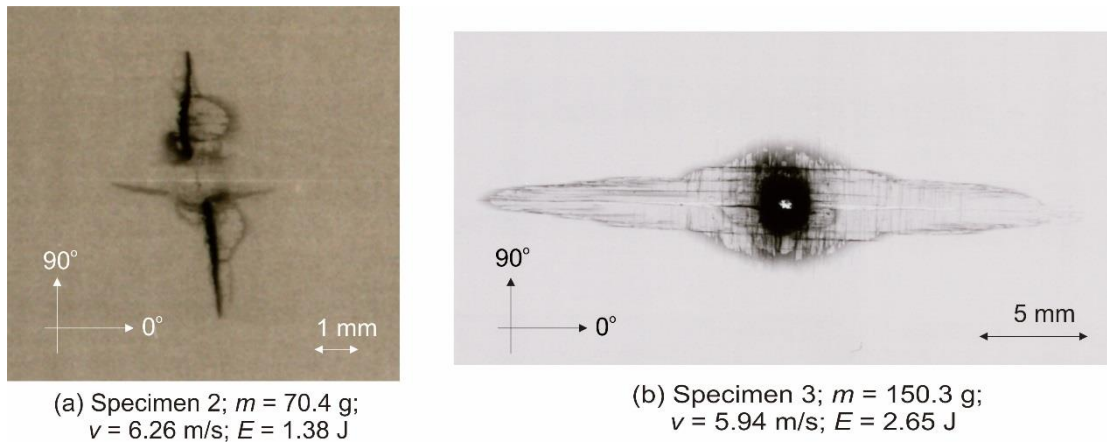
Figure 5.10: Soft X-ray photographs of the laminates after low-velocity impact for specimen 2 and specimen 3.

In addition, the delamination area is plotted against the impact energy as depicted in Figure 5.11 and it indicates the delamination area increases with the increase of impact energy. Additionally, the threshold energy is approximately 0.18 J as stated in [65].
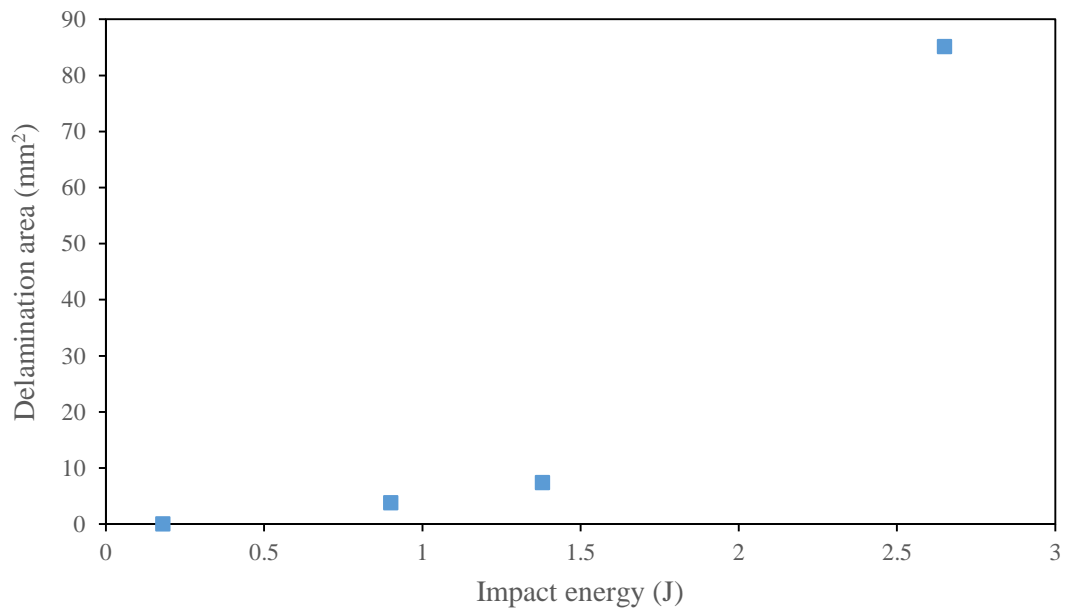
Figure 5.11: The delamination area is plotted against the impact energy.

5.5   Deflection of the Laminate

Figure 5.12 compares the deflection-time curve between the experiment result and

the simulations with and without considering intralaminar delamination. The calculation

in the former case was terminated before reaching the maximum deflection because the

failed elements in the base plies are largely distorted. The deflection rate of the former

case gives fairly good agreement with the experiment result up to 0.0003 s approximately.

Since most of the damage are generated by this time, the simulation is successful as far

as the damage prediction is concerned. As a result, it can be said that the prediction with

intralaminar delamination provides better agreement with the experiment result.
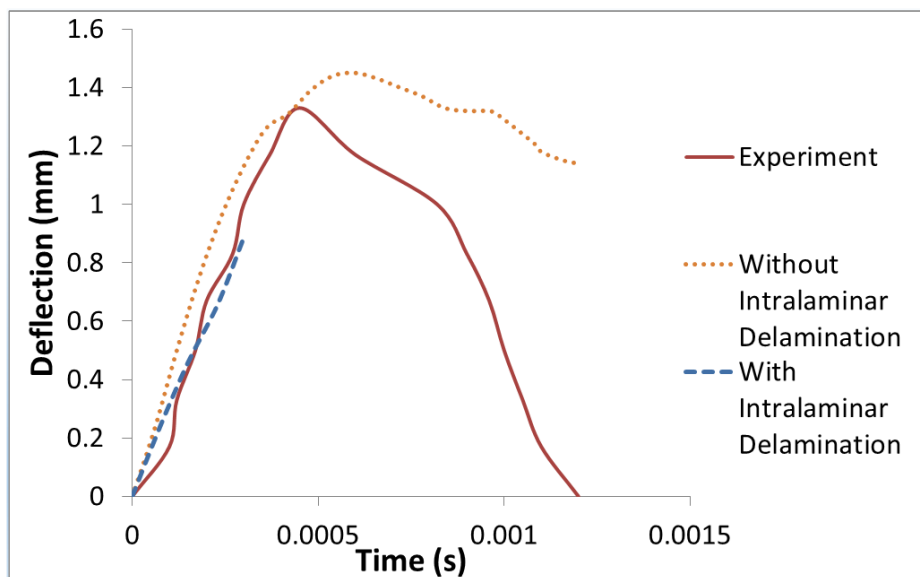
Figure 5.12: Measured and predicted time history of deflection of specimen 1 [66].

In addition, the deflection of the laminate for other impact velocities is plotted against

time graph in Figure 5.13. From the figure, the laminate deflects both in linear and non-linear trend. The deflection is at a faster rate as the speed of impactor increased and the maximum deflection occurs in between 0.4 ms to 0.5 ms.

Figure 5.14 depicts the maximum deflection at the center of the laminate after subjected to impact at different incident impact energy for two types of impactor masses. The deflection increases as the impact energy becomes greater. However, for the mass of 150.3 g, the deflection decreases at the impact energy of 2.92 J due to penetration on the laminate.
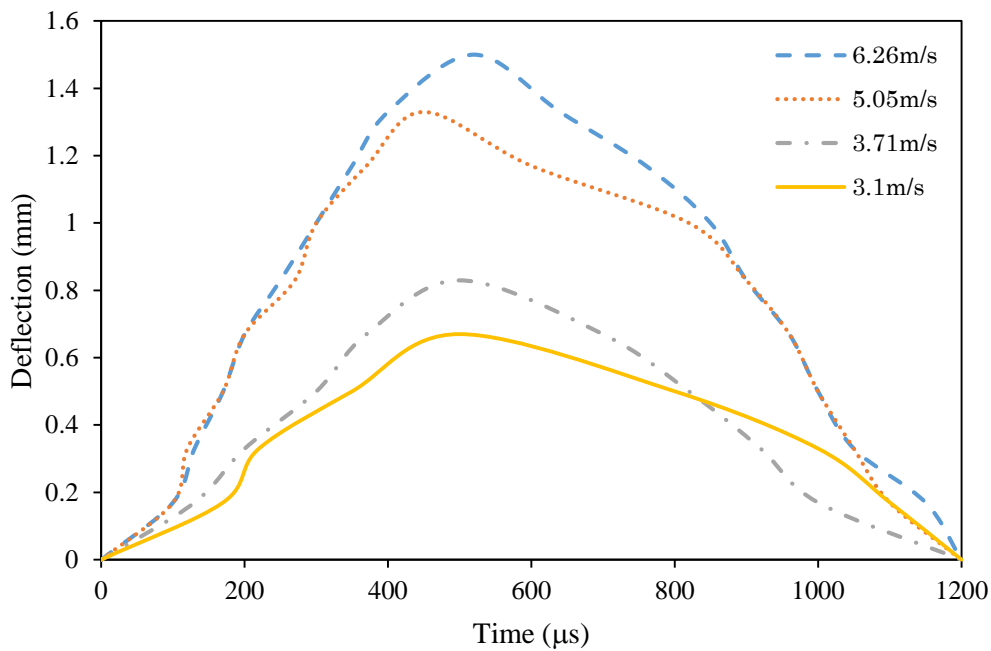
Figure 5.13: Time history of deflection via experimental characterization.
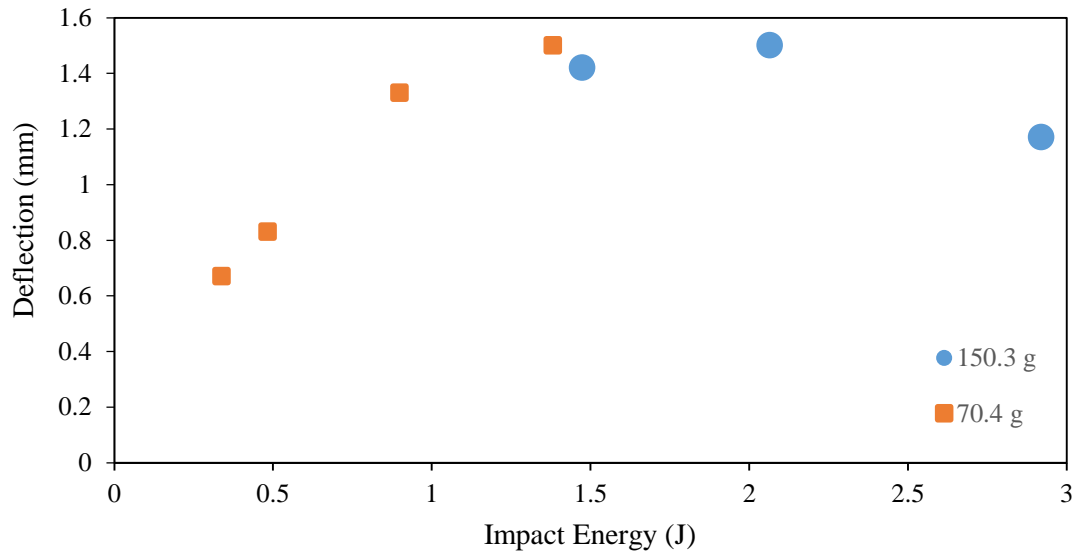
Figure 5.14: Relationship between deflection and impact energy for two masses; (a) 70.4g and (b) 150.3g.

5.6 Summary of the Chapter

The low-velocity impact damage of a CFRP laminate with toughened interlayers was experimentally and numerically characterised in this chapter. Based on the results obtained, it can be summarized as follows:

1. The cracks on the front surface are generated due to high compressive stress in the 0°-direction during the impact, whereas not only the interlaminar but also the intralaminar delaminations are generated inside the laminate.

2. The present numerical simulation can reproduce the damage pattern including intralaminar delamination.

3. The simulation considering both interlaminar and intralaminar delaminations gives

better agreement with the experiment result of the deflection rate in the deflection-

time curve.

CHAPTER 6: CONCLUSIONS AND FUTURE WORKS

The microscopic damage of CFRP with toughened interlayers when subjected to low- and high-velocity impacts has been successfully characterized via experimental characterization and numerical modelling. The general conclusions throughout all the chapters can be summarized as follows:

1. The damage mechanisms of the laminate is relatively similar when subjected to low- and high-velocity impacts. Nevertheless, the degree of damage at the vicinity impact point due to high-velocity impact is greater than low-velocity impact since high-velocity impact generates localized deformation. On the other hand, the energy dissipation due to low-velocity impact damage is widely distributed to a wide area of the laminate. Thus, the degree of damage is relatively mild.

2. The toughened interlayers acts as crack arrestor to suppress delamination propagation when the incident impact energy is below a threshold value (as in this study 0.18J). In addition, the high fracture toughness of the interlayers sometimes produces transition of the interlaminar delamination to intralaminar delamination.

3. The current numerical modelling by introducing intralaminar delamination coupled with interlaminar delamination provides better damage prediction and agreement with experimental results.

4. The novel finding in this research is the generation of intralaminar delamination for this type of laminate which is different from conventional CFRP laminate as this type of damage is not observed in conventional CFRP laminate. Furthermore, the insertion of cohesive elements in numerical model to model both intralaminar delamination and interlaminar delamination provides better result than the simulation with interlaminar delamination only.

Finally, several recommendations are suggested to further study the impact response of CFRP with toughened interlayers as follows:

1. Parametric study on the effect of material properties of interlayers when subjected to impact loading.

2. Comparison of the damage between low-velocity impact and quasi-static indentation test.

3. Numerical modelling of high-velocity impact on the laminate.

4. Parametric study on the effect of number of plies as well as stacking sequence of

the laminate when subjected to impact loading.

REFERENCES

[1]   C. Soutis, "Carbon fiber reinforced plastics in aircraft construction," *Mater. Sci. Eng. A*, vol. 412, pp. 171–176, 2005.

[2]   M. Hojo, Y. Hirose, T. Kusaka, and M. Nishikawa, "Recent Advances in Carbon Fiber Reinforced Plastics," in *Third International Conference on Sustainable Construction Materials and Technologies*, 2013.

[3]   W. G. Roeseler, B. Sarh, and M. U. Kismarton, "Composite Structures : The First 100 Years," in *16th International Conference on Composite Materials*, 2007, pp. 1–10.

[4]   "Boeing 787 Dreamliner Specs - Modern Airliners." [Online]. Available: http://www.modernairliners.com/boeing-787-dreamliner/boeing-787-dreamliner-specs/.

[5]   D. Paul, L. Kelly, V. Venkayya, U. S. N. Air, S. Command, and P. River, "Evolution of U . S . Military Aircraft Structures Technology Introduction," *J. Aircr.*, vol. 39, no. 1, pp. 18–29, 2002.

[6]   M. Hojo, T. Ando, M. Tanaka, T. Adachi, S. Ochiai, and Y. Endo, "Modes I and II interlaminar fracture toughness and fatigue delamination of CF/epoxy laminates with self-same epoxy interleaf," *Int. J. Fatigue*, vol. 28, no. 10 SPEC.

ISS., pp. 1154–1165, 2006.

[7]   S. H. Lee, H. Kim, S. Hang, and S. K. Cheong, "Interlaminar fracture toughness of composite laminates with CNT-enhanced nonwoven carbon tissue interleave," *Compos. Sci. Technol.*, vol. 73, no. 1, pp. 1–8, Nov. 2012.

[8]   N. Odagiri, H. Kishi, and M. Yamashita, "Development of TORAYCA prepreg P2302 carbon fiber reinforced plastic for aircraft primary structural materials," *Adv. Compos. Mater.*, vol. 5, no. October, pp. 249–254, 1996.

[9]   D. Brosius, "Boeing 787 Update," 2007. [Online]. Available: http://www.compositesworld.com/articles/boeing-787-update.

[10]   W. J. Cantwell and J. Morton, "Comparison of the low and high velocity impact response of CFRP," *Composites*, vol. 20, no. 6, pp. 545–551, 1989.

[11]   H. Morita, A. K. Hamamoto, and T. Hiroyuki, "Characterization of Impact Damage Resistance of CF, PEEK and CF, Toughened Epoxy Laminates under Low and High Velocity Impact Tests," *J. Soc. Mater. Sci. Japan*, vol. 44, no. 499, pp. 423–427, 1995.

[12]   H. Morita, H., Adachi, T., Tateishi, Y. and Matsumoto, "Characterization of impact damage resistance of CF/PEEK and CF/Toughened epoxy laminates under low and high velocity impact tests," *J. Reinf. Plast. Compos.*, vol. 16, no.

2, pp. 131–143, 1997.

[13] D. D. R. Cartié and P. E. Irving, "Effect of resin and fibre properties on impact and compression after impact performance of CFRP," *Compos. - Part A Appl. Sci. Manuf.*, vol. 33, no. 4, pp. 483–493, 2002.

[14] R. Hosseinzadeh, M. M. Shokrieh, and L. Lessard, "Damage behavior of fiber reinforced composite plates subjected to drop weight impacts," *Compos. Sci. Technol.*, vol. 66, no. 1, pp. 61–68, 2006.

[15] B. Vieille, V. M. Casado, and C. Bouvet, "About the impact behavior of woven-ply carbon fiber-reinforced thermoplastic- and thermosetting-composites: A comparative study," *Compos. Struct.*, vol. 101, pp. 9–21, 2013.

[16] M. De Freitas and L. Reis, "Failure mechanisms on composite specimens subjected to compression after impact," *Compos. Struct.*, vol. 42, no. 4, pp. 365–373, 1998.

[17] S.-X. Wang, L.-Z. Wu, and L. Ma, "Low-velocity impact and residual tensile strength analysis to carbon fiber composite laminates," *Mater. Des.*, vol. 31, no. 1, pp. 118–125, 2010.

[18] J.-M. Koo, J.-H. Choi, and C.-S. Seok, "Prediction of post-impact residual strength and fatigue characteristics after impact of CFRP composite structures,"

Compos. Part B Eng., vol. 61, pp. 300–306, 2014.

[19]   E. N. Gilbert, B. S. Hayes, and J. C. Seferis, "Interlayer toughened unidirectional

carbon prepreg systems: Effect of preformed particle morphology," *Compos.*

Part A Appl. Sci. Manuf., vol. 34, no. 3, pp. 245–252, 2003.

[20]   D. J. Bull, A. E. Scott, S. M. Spearing, and I. Sinclair, "The influence of

toughening-particles in CFRPs on low velocity impact damage resistance

performance," *Compos. Part A Appl. Sci. Manuf.*, vol. 58, pp. 47–55, Mar. 2014.

[21]   M. Yasaee, I. P. Bond, R. S. Trask, and E. S. Greenhalgh, "Damage control using

discrete thermoplastic film inserts," *Compos. Part A Appl. Sci. Manuf.*, vol. 43,

no. 6, pp. 978–989, Jun. 2012.

[22]   X. Xu, Z. Zhou, Y. Hei, B. Zhang, J. Bao, and X. Chen, "Improving

compression-after-impact performance of carbon–fiber composites by

CNTs/thermoplastic hybrid film interlayer," *Compos. Sci. Technol.*, vol. 95, pp.

75–81, May 2014.

[23]   R. Palazzetti, A. Zucchelli, and I. Trendafilova, "The self-reinforcing effect of

Nylon 6,6 nano-fibres on CFRP laminates subjected to low velocity impact,"

Compos. Struct., vol. 106, pp. 661–671, Dec. 2013.

[24]   Y. Shi, C. Pinna, and C. Soutis, "Modelling impact damage in composite

laminates: A simulation of intra- and inter-laminar cracking," *Compos. Struct.*, vol. 114, pp. 10–19, Aug. 2014.

[25] S. Xu and P. H. Chen, "Prediction of Low Velocity Impact Damage in carbon/epoxy Laminates," *Procedia Eng.*, vol. 67, pp. 489–496, Jan. 2013.

[26] D. Feng and F. Aymerich, "Finite element modelling of damage induced by low-velocity impact on composite laminates," *Compos. Struct.*, vol. 108, pp. 161–171, Feb. 2014.

[27] N. Hongkarnjanakul, C. Bouvet, and S. Rivallant, "Validation of low velocity impact modelling on different stacking sequences of CFRP laminates and influence of fibre failure," *Compos. Struct.*, vol. 106, pp. 549–559, Dec. 2013.

[28] M. May, M. Nossek, N. Petrinic, S. Hiermaier, and K. Thoma, "Adaptive multi-scale modeling of high velocity impact on composite panels," *Compos. Part A Appl. Sci. Manuf.*, vol. 58, pp. 56–64, Mar. 2014.

[29] ABAQUS, "Abaqus User's Guide Version 6.14." 2014.

[30] K. Shigemori, A. Hosoi, Y. Fujita, and H. Kawada, "Fatigue strength properties of interlaminar toughened CFRP laminates under cyclic loading in the out-of-plane direction," *Trans. JSME (in Japanese)*, vol. 80, no. 812, p. SMM0087-SMM0087, 2014.

[31]   A. Creations, "MatWeb: Online Materials Information Resource," *Internet*. p. , 2010.

[32]   K. Ogi, S. Yashiro, and A. Yoshimura, "CFRP High-Velocity Impact Damage in CFRP Unidirectional and Cross-Ply Laminates by," *J. Soc. Mater. Sci. Japan*, vol. 60, no. 5, pp. 418–424, 2011.

[33]   S. Yashiro, K. Ogi, A. Yoshimura, and Y. Sakaida, "Characterization of high-velocity impact damage in CFRP laminates: Part II − prediction by smoothed particle hydrodynamics," *Compos. Part A Appl. Sci. Manuf.*, vol. 56, pp. 308–318, Jan. 2014.

[34]   T. Morimoto, S. Sugimoto, H. Katoh, E. Hara, T. Yasuoka, Y. Iwahori, T. Ogasawara, and S. Ito, "JAXA Research and Development Memorandum," Tokyo, Japan, 2015.

[35]   P. Camanho and C. G. Davila, "Mixed-Mode Decohesion Finite Elements in for the Simulation Composite of Delamination Materials," *Nasa*, vol. TM-2002-21, no. June, pp. 1–37, 2002.

[36]   M. L. Benzeggagh and M. Kenane, "Measurement of mixed-mode delamination fracture toughness of unidirectional glass/epoxy composites with mixed-mode bending apparatus," *Compos. Sci. Technol.*, vol. 56, no. 4, pp. 439–449, 1996.

[37] S. Abrate, "Impact on laminated composite materials," *Appl. Mech. Rev.*, vol. 44, no. 4, pp. 155–190, 1991.

[38] S. Abrate, "Impact on Laminated Composites: Recent Advances," *Applied Mechanics Reviews*, vol. 47, no. JANUARY 1994. p. 517, 1994.

[39] S. Abrate, *Impact on Composite Structures*. New York: Cambridge University Press, 1998.

[40] W. Goldsmith, C. Dharan, and H. Chang, "Quasi-Static and Ballistic Perforation of Carbon Fiber Laminates," *Int. J. Solids Struct.*, vol. 32, no. 1, pp. 89–103, 1995.

[41] J. López-Puente, R. Zaera, and C. Navarro, "Experimental and numerical analysis of normal and oblique ballistic impacts on thin carbon/epoxy woven laminates," *Compos. Part A Appl. Sci. Manuf.*, vol. 39, no. 2, pp. 374–387, 2008.

[42] Y. Tanabe, M. Aoki, K. Fujii, H. Kasano, and E. Yasuda, "Fracture behavior of CFRPs impacted by relatively high-velocity steel sphere," *Int. J. Impact Eng.*, vol. 28, no. 6, pp. 627–642, 2003.

[43] P. J. Hazell, G. Kister, C. Stennett, P. Bourque, and G. Cooper, "Normal and oblique penetration of woven CFRP laminates by a high velocity steel sphere," *Compos. Part A Appl. Sci. Manuf.*, vol. 39, no. 5, pp. 866–874, 2008.

[44] T. Mitrevski, I. H. Marshall, R. Thomson, R. Jones, and B. Whittingham, "The effect of impactor shape on the impact response of composite laminates," *Compos. Struct.*, vol. 67, no. 2 SPEC. ISS., pp. 139–148, 2005.

[45] S. Heimbs, S. Heller, P. Middendorf, F. Hähnel, and J. Weiße, "Low velocity impact on CFRP plates with compressive preload: Test and modelling," *Int. J. Impact Eng.*, vol. 36, no. 10–11, pp. 1182–1193, 2009.

[46] K. A. Dransfield, L. K. Jain, and Y.-W. Mai, "On the effects of stitching in CFRPs—I. mode I delamination toughness," *Compos. Sci. Technol.*, vol. 58, no. 6, pp. 815–827, 1998.

[47] L. K. Jain, K. A. Dransfield, and Y.-W. Mai, "On the effects of stitching in CFRPs—II. Mode II delamination toughness," *Compos. Sci. Technol.*, vol. 58, no. 6, pp. 829–837, 1998.

[48] M. R. Parlapalli, K. C. Soh, D. W. Shu, and G. Ma, "Experimental investigation of delamination buckling of stitched composite laminates," *Compos. Part A Appl. Sci. Manuf.*, vol. 38, no. 9, pp. 2024–2033, 2007.

[49] S. N. Yadav, V. Kumar, and S. K. Verma, "Fracture toughness behaviour of carbon fibre epoxy composite with Kevlar reinforced interleave," *Mater. Sci. Eng. B Solid-State Mater. Adv. Technol.*, vol. 132, no. 1–2, pp. 108–112, Jul.

2006.

[50]   D. W. Y. Wong, L. Lin, P. T. McGrail, T. Peijs, and P. J. Hogg, "Improved

        fracture toughness of carbon fibre/epoxy composite laminates using dissolvable

        thermoplastic fibres," *Compos. Part A Appl. Sci. Manuf.*, vol. 41, no. 6, pp. 759–

        767, 2010.

[51]   H. Saghafi,   a. Zucchelli, R. Palazzetti, and G. Minak, "The effect of interleaved

        composite nanofibrous mats on delamination behavior of polymeric composite

        materials," *Compos. Struct.*, vol. 109, no. 1, pp. 41–47, Mar. 2014.

[52]   H. Ito, M. Arai, K. Takeyama, and N. Hu, "Impact Damage and Residual

        Compression Strength of CNF / CFRP Hybrid Laminates *," *J. Solids Mech.

        Mater. Eng.*, vol. 7, no. 3, pp. 381–393, 2013.

[53]   S. Yashiro, K. Ogi, T. Nakamura, and A. Yoshimura, "Characterization of high-

        velocity impact damage in CFRP laminates: Part I – Experiment," *Compos. Part

        A Appl. Sci. Manuf.*, vol. 48, pp. 93–100, May 2013.

[54]   V. V. Silberschmidt, *Dynamic Deformation, Damage and Fracture in Composite

        Materials and Structures*. 2016.

[55]   P. M. Moran, X. H. Liu, and C. F. Shih, "Kink band formation and band

        broadening in fiber composites under compressive loading," vol. 43, no. 8, pp.

2943–2958, 1995.

[56] S. Narayanan and L. S. Schadler, "Mechanisms of kink-band formation in

graphite/epoxy composites: A micromechanical experimental study," *Compos.*

Sci. Technol., vol. 59, no. 15, pp. 2201–2213, 1999.

[57] D. Delfosse and A. Poursartip, "Energy-based approach to impact damage in

CFRP laminates," *Compos. Part A Appl. Sci. Manuf.*, vol. 28, no. 7, pp. 647–655,

1997.

[58] M. Hojo, S. Matsuda, M. Tanaka, S. Ochiai, and A. Murakami, "Mode I

delamination fatigue properties of interlayer-toughened CF/epoxy laminates,"

Compos. Sci. Technol., vol. 66, no. 5, pp. 665–675, May 2006.

[59] M. O. . Richardson and M. . Wisheart, "Review of low-velocity impact properties

of composite materials," *Compos. Part A*, vol. 27A, pp. 1123–1131, 1996.

[60] G. a. O. Davies and X. Zhang, "Impact damage prediction in carbon composite

structures," *Int. J. Impact Eng.*, vol. 16, no. 1, pp. 149–170, 1995.

[61] T.-W. Shyr and Y.-H. Pan, "Impact resistance and damage characteristics of

composite laminates," *Compos. Struct.*, vol. 62, no. 2, pp. 193–203, Nov. 2003.

[62] P. S. S. Gouda, S. K. Kudari, S. Prabhuswamy, and D. Jawali, "Fracture

Toughness of Glass-Carbon (0 / 90) S Fiber Reinforced Polymer Composite −

An Experimental and Numerical Study," vol. 10, no. 8, pp. 671–682, 2011.

[63] Q. Meng and Z. Wang, "Micromechanical Modeling of Impact Damage Mechanisms in Unidirectional Composite Laminates," *Appl. Compos. Mater.*, vol. 23, no. 6, pp. 1099–1116, 2016.

[64] M. Nishikawa, T. Okabe, and N. Takeda, "Numerical simulation of interlaminar damage propagation in CFRP cross-ply laminates under transverse loading," *Int. J. Solids Struct.*, vol. 44, no. 10, pp. 3101–3113, 2007.

[65] R. Othman, K. Ogi, and S. Yashiro, "Characterization of microscopic damage due to low-velocity and high-velocity impact in CFRP with toughened interlayers," *Mech. Eng. J.*, vol. 3, no. 6, pp. 16–00151, 2016.

[66] R. Othman, K. Ogi, K. Mizukami, and S. Yashiro, "Experimental and Numerical Characterization of Low-Velocity Impact Damage of a CFRP Laminate with Interlayers," *Mater. Syst.*, vol. 35, pp. 29–35, 2017.